Rainwater Infiltration Model of the Chocaya Basin using Hydrus-1D

Alexander Bergman
Mire Persmark

Division of Engineering Geology
Faculty of Engineering
Lund University

Thesis work for Masters in Science 30 ECTS
Engineering Geology, LTH, Lund University

Title: Rainwater Infiltration Model of the Chocaya Basin using Hydrus-1D

Alexander Bergman
Mire Persmark

Engineering Geology
Faculty of Engineering
Lund University

Lund 2020

LUTVDG/ (TVTG-5164)/1-42/(2020)

Acknowledgements

Abstract

The objective of this study was to assess the rainwater infiltration process in the unsaturated zone in an alluvial plain. Particularly, this study is focused on the Chocaya basin in central Bolivia.

The hydraulic conductivity (K_{f_s}) was obtained from seven in situ measurements of infiltration rate (I) performed by Double Ring Infiltrometer (DRI) test. These seven values were compared to the hydraulic conductivity (K_s) obtained from the empirical models; Hazen equation, Beyer equation and the Rosetta module based on particle size distribution (PSD) data obtained from soil samples. The hydraulic conductivity ranged from 3.4×10^{-8} to 2.3×10^{-1} m/s.

The obtained soil parameters were implemented with collected meteorological data in Hydrus-1D to simulate the soil water content through a 5m deep soil column. Electrical resistivity tomography (ERT) was used to assess the sub-surface soil structure. The performance of the infiltration model simulating soil water content was compared to in situ observations from soil moisture sensors.

The results implied that the hydraulic conductivity obtained from the double ring infiltrometer test and the Rosetta module manage to recreate the soil water content better than values from the Hazen and Beyer equations.

The Hydrus-1D models were built to represent the alluvial plain during a 14-months period (2018–2020) to cover a complete rain season and dry season. According to the simulation result, the bottom flux ranges between 0-15 cm yearly through the 5m soil profile. The model results are largely dependent on initial soil water content (θ_i) and saturated hydraulic conductivity (K_s). This demonstrate the importance of obtaining good field investigation parameters.

The study showed that using laboratory-determined soil hydraulic properties to simulate the soil water content at field scale in a stratified soil can produce inaccurate results.

Table of Contents

Abbreviations

DRI	Double Ring Infiltrometer
ERT	Electrical Resistivity Tomography
ET_0	Evapotranspiration
FM1	Field Model 1
FM2	Field Model 2
GW	Groundwater
GWR	Groundwater Recharge
HG	The Hargreaves Equation
IM1	Inverse Model 1
IM2	Inverse Model 2
K_s	Saturated Hydraulic Conductivity
PM	The Penman-Monteith Equation
PSD	Particle Size Distribution
θ	Soil Water Content
θ_i	Initial Soil Water Content
ϕ	Porosity
ρ	Electrical Resistivity
Θ_{fc}	Field Capacity
Θ_r	Residual Water Content
Θ_s	Saturated Water Content
Θ_{wp}	Wilting Point

1. Introduction

The rapid population growth and economic development in developing countries implies a challenge in accomplishing the United Nations (UN) Sustainable Development Goal number six (SDG 6); to ensure clean and accessible water and sanitation for all. There is a close relationship that links water access to poverty (Ohlsson, 2000). Therefore, a long-term sustainable management of water resources will help to ensure water and food security, which are key factors creating sustainable communities (UN. Secretary-General, 2018).

1.1 Bolivia

The Plurinational State of Bolivia is one of the poorest countries in South America suffering from major social and uneven economic development within the country (UI, 2019). Bolivia has 28,300 m^3 of renewable internal freshwater resources per capita as can be compared with 17,600 m^3 per capita in Sweden (AQUASTAT, 2020). However, this asset is not homogeneously distributed across the country. Instead the distribution reflects the country's characteristic geography with eastern Bolivia receiving most precipitation. Up to 5000mm/year while the western part of Bolivia, characterized by its arid or semi-arid climate, can have an annual precipitation of as little as 10 mm. Generally, 80 % of the precipitation falls during the rainy season (November-April) while during the dry season (June-October), the precipitation rate is low. This annual and spatial variation in the hydrological cycle causes problems with sufficient water access nationally over the year (Renner et al., 2000). Therefore, adequate management of water resources is necessary for improving welfare in rural regions. This becomes even more evident in arid and semiarid regions due to water access restrictions (Cossio et al., 2010)

1.2 Central Valley of Cochabamba

The field study was performed in the central valley of Cochabamba in the Chocaya basin. The department of Cochabamba is situated in the central part of Bolivia in the sub-Andean valley (Figure 1) (Gonzales Amaya et al., 2018). The population is approximately 1,900,000 inhabitants (INE, 2016) and has observed a rapid population growth in the last decades. This has increased the water demand mainly for human consumption and irrigation, thus putting a challenge to the available water resources. The most important water resource has been over decades groundwater extraction from aquifers which as per 2012 provided 65 % of the water supply in Cochabamba valley (MMAyA, 2014). However, due to unsustainable exploitation the groundwater has shown a decreasing trend and an inability to satisfy the regions increasing demand (DGIA, 2014). The construction of the Misicuni dam, which is a large-scale water supply system in the department, started in 2009 in order to cope with the increasing water scarcity in Cochabamba valley (MMAyA, 2014. The dam is operating since 2018, however, the water is not used for consumption as the construction of water distribution networks is absent implying that the protection of aquifers and recharge areas is highly important (Gonzales Amaya, 2019)
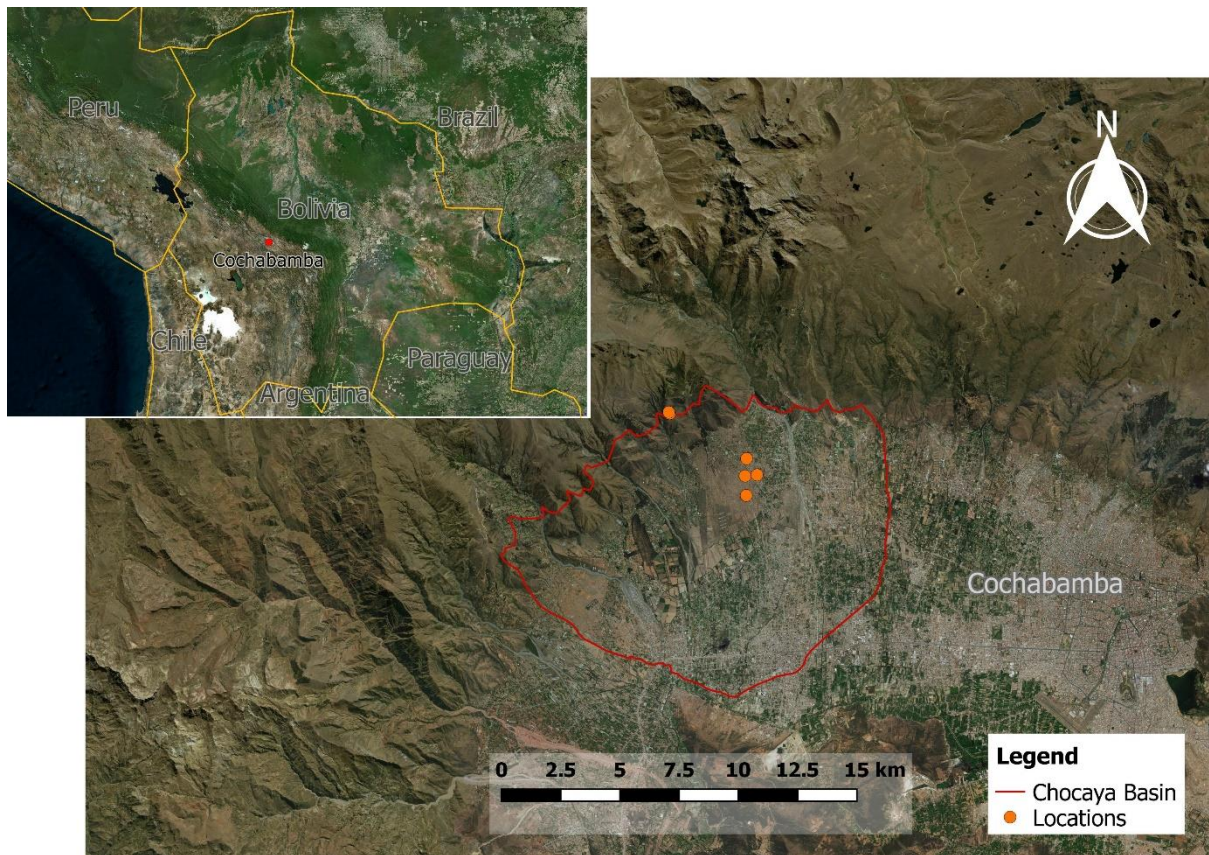
Figure 1. Map of Bolivia with the central valley of Cochabamba. Chocaya basin is marked with a red line and the sampling sites are marked with orange dots.

1.3 Aim & Objectives

The aim of this project is to obtain a greater understanding of the infiltration by precipitation processes in Chocaya basin. The interest lies in this alluvial plain and its recharge potential to underlying aquifers. This report may further encourage a more sustainable water resources management to increase living standards and raise economic growth. It is a contribution to an eventually complete water balance model of the Chocaya basin.

The objectives of this project are to:
- Estimate the infiltration rate with a double ring infiltrometer (DRI) in the Chocaya basin.
- Estimate the hydraulic conductivity from DRI tests and compare to values obtained from empirical equations by Hazen and Beyer and to the Rosetta module.
- Use Electrical Resistivity Tomography (ERT) to map the near-surface soil layers.
- Build a representative infiltration model of the Chocaya basin in Hydrus-1D.

1.4 Geology and Hydrogeology

The central valley of Cochabamba is a plain surrounded by mountain ranges (Figure 1). It exhibits large differences in altitude where the highest peak in the Tunari mountain range to the north have an elevation of 5,030 m whereas the lowest elevation of the southern part of the plain measures 2,470 m. The average elevation of the plain in the central part of the basin is 2,600 m. The central valley of Cochabamba has semi-arid climate with an average annual temperature of 17.5 °C. The average annual precipitation is moderate, 400-500 mm. This climate result in that the region has a relatively high potential evapotranspiration (Renner et

2

al., 2000; World Weather Online, 2019). The regional geological feature is the Tunari mountain range in the northern and western part flanking the central valley that are composed of Palaeozoic and Cretaceous rocks. The most extensive unconsolidated geological unit is alluvial Quaternary sediment that expose a large variation in grain size due to a complex depositional process. The plain of the valley is a tectonic basin that was once a lake. As a result, the deepest part of the valley is composed of lake deposits with sedimentary filling. Over the years the size of the lake has fluctuated. Times of large areal extension has led to sediment deposition of lacustrine clay in the basin. During periods when the lake was reduced in size, a flat landscape was exposed which is characteristic of lacustrine plains. Rivers, arising in the northern and western mountain range meandered through the plain where they deposit thick alluvial material of different generations along their course. This led to the formation of deposits of alluvial cones mainly along the northern and western part of the basin. These fans are to the greatest extent formed during the wet season when torrents increase the water volume which transport large quantities of material that deposits at the foot of the mountains. The lake has then again increased in extent once again covering the plain with water thus depositing fine lake sediments on the alluvial plain in the deepest parts of the basin (Renner et al., 2000).

1.5 Study Area: Chocaya Basin

The Chocaya basin has an approximate area of 100 km^2 and is predominantly an agricultural region. In the middle part of the basin an alluvial plain is located which extends over 1km^2. This area will further in this report be referred to as the plain. The topography is mainly gently sloping at an altitude of approximately 2,600 m.a.s.l. The thickness of the unconsolidated sediment in the basin range from a few meters to hundreds of meters and several deep wells (~300 m) that supply Cochabamba with fresh water have been drilled in the alluvial plain (Renner et al., 2000). However, Chocaya basin observes a rapid urbanization and there is an apprehension that an exploitation of the flood plains can causes a potential threat to the available water sources. The anthropogenic activities might cause consequences such as groundwater pollution and decrease in groundwater recharge (Gonzales Amaya, 2019).

This study attempts to investigate the area's potential for rainwater infiltration into groundwater as alluvial fans are known for their positive groundwater replenishment. If an infiltration potential can be established it can be used as a base for a future management plan of water resources of Cochabamba valley. Two separate sites in the alluvial fan in Chocaya basin were chosen as sample areas (Figure 2). The selection of the areas was predominantly determined from where permission of landowners could be obtained. Additionally, they were based on the absence of obstacles such as houses, fences and crops.

Site 1 - Location 1 and 2 are located in the outskirt of the Chocaya basin.

Site 2 - Location 3, 4 and 6 are located in the central part of the Chocaya basin. Location 5 is situated on a riverbed that runs through the area.

Figure 2. Chocaya basin with numbered sample Locations (orange dots).

2. Theory

2.1 Groundwater Recharge (GWR)

The natural recharge process of groundwater in a region depends on several factors such as local topography, spatial and temporal distribution of rainfall, properties of the unsaturated zone and depth to the groundwater table. Natural groundwater recharge (GWR) can be diffuse or localized. Diffuse recharge is infiltration and percolation of precipitation or irrigation through the unsaturated zone to the groundwater table. Localized recharge is movement of water from surface water bodies to the groundwater. Most groundwater systems receive both diffuse and localized recharge. There is, however, a high variability of precipitation that generates diffuse recharge. In general, the importance of diffuse recharge process decreases with an increase of a region's aridity. (Alley, 2009; Şen, 2015)

Groundwater models play an important role in understanding regional groundwater recharge (GWR) processes. Estimation methods include use of water budgets, tracers and simulation models. Because estimation methods often hold inherent uncertainties, GWR can be hard to predict (Scanlon et al., 2002). A previous study by Gonzales Amaya et al. (2018) examined the GWR processes in the Punata alluvial fan, with proximate geographic location to the Chocaya basin. They demonstrated that vertical infiltration is of minor importance for recharge processes presumable due to semipermeable lenses in the subsoil.

2.2 Electrical Resistivity Tomography (ERT)

Electrical Resistivity Tomography (ERT), is a widely used geoelectrical method for mapping near-surface layers of the soil along profiles since the electrical resistivity (ρ) of the ground varies with water content and lithology (Dahlin, 2001). The main method uses a known current (I) that is induced in the ground using two current electrodes (C1, C2). The electrical potential difference (ΔV) is then read using two potential electrodes (P1, P2) (Figure 3) (Hung et al., 2019). The process is implemented repeatedly with different electrode configurations to generate a spatial model of vertical and lateral variations to obtain the electrical resistivity of the subsurface. There are many electrode array configurations available with different practical applicability (Reichling et al., 2015).
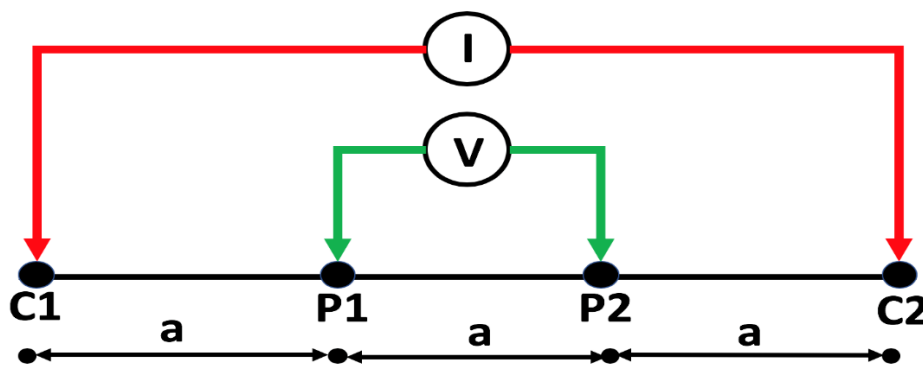
Figure 3. A schematic figure over a Wenner electrode configuration setup. The red and green arrows represent current respectively potential electrodes.

The Gradient array setup (Figure 4) has been found to yield a high data density due to an increase in speed of data acquisition in field. Additionally, it is giving a good horizontal resolution which is favourable when trying to detect subsurface layers (Bing, 2019). A current electrode separation of $(n + 2)a$ is used to inject the current in the subsoil where n is the

separation factor and *a* is the spacing between the potential electrodes . The potential electrodes measure all the corresponding voltages (Aning et al., 2013).
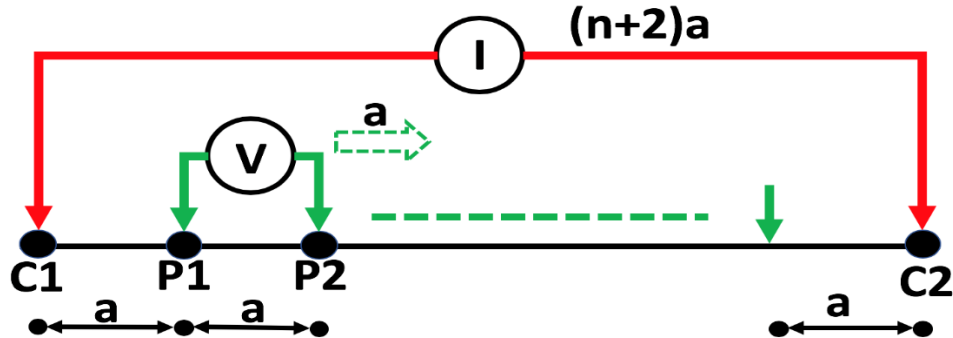
Figure 4. The Gradient array setup with a current-electrode separation of (n+2)a. C1 and C2 are the current electrodes, while P1 and P2 are the potential electrodes.

The measured resistivity is called apparent resistivity. However, this cannot be interpreted as the true resistivity of the subsoil as in electrical resistivity tomography (ERT) it is assumed that the geological resistivity of the subsoil properties is vertically homogeneous which is generally not the case (Hung et al., 2019). Instead an estimation of the true resistivity is obtained by performing an inverse numerical modelling process (inversion) on the apparent resistivity values. The inversion adjusts a finite element model in an iterative process by comparing the measured apparent resistivity versus the calculated resistivity from the inverted model (Hung et al., 2019).

2.3 Double Ring Infiltrometer (DRI)

The double ring infiltrometer is an instrument used for measuring water infiltration of the soil. It consists of two cylinders that are partially inserted to the soil that are both filled up to an equal level with water (Figure 5)(Soilmoisture Equipment Corp., 2009). The inner cylinder is for measurement and the outer cylinder reduces the error caused by lateral flow (Fatehnia et al., 2016). This test method has proven to be particularly applicable to soils with characteristics of being relatively uniform fine-grained, without plastic clays and gravel-size particles (Soilmoisture Equipment Corp., 2009). The minimum cylinder diameters required to get accurate results have been studied by several researchers. It is summarised in a study by Fatehnia et al. (2016) where the recommended diameter for inner/outer cylinder ranges between 0.15/0.3 m to 0.8/1.0 m.
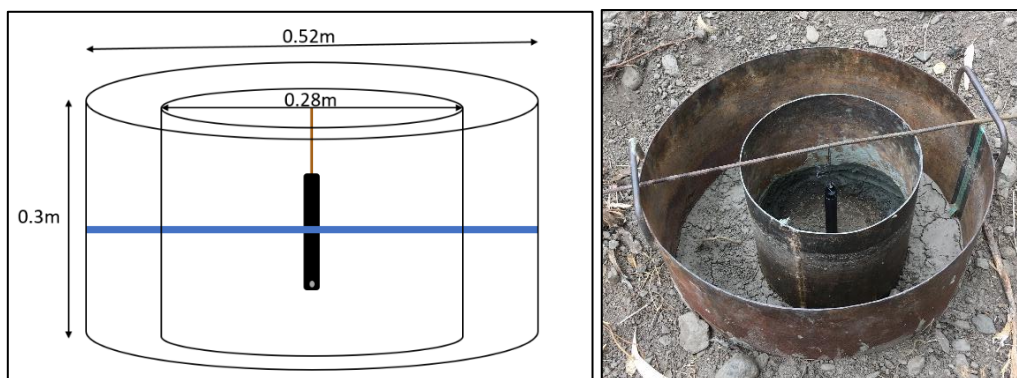
Figure 5. Schematic sketch (left) and picture (right) of the double ring infiltrometer with a level logger installed inside the inner ring.

2.4 Hydraulic Conductivity

The saturated hydraulic conductivity (K_s) in soil is a crucial parameter when estimating and modelling fluids movement in soil. It is a physical property of the ability to transmit fluids in soils and rocks. Although important, it is considered a difficult parameter to determine in-situ due to natural soil heterogeneity (Shiraki et al., 2019). There are empirical methods based on soil parameters and viscosity of the fluid (Wang et al., 2017) to approximate K_s such as the Hazen model and the Beyer model. There are experimental methods which are conducted either in a lab or in-situ. The experimental models to estimate K_s are empirical equations derived from Richard's equation for one-dimensional, isothermal, non-hysteretic water flow in non-swelling soils (Mollerup, 2007). Examples of such models are the Philip's infiltration model, Horton's infiltration model and the Green Ampt method. The Philip's model was chosen as it is easy to use and has previously been used in the area by the Universidad Major de San Simon (UMSS). During infiltration tests in the field only near-saturated conductivity (K_{ns}) can be estimated because of voids in the soil filled with air. In this report, the voids are assumed to have little effect in comparison to other sources of error hence K_{ns} are assumed to be equal to K_s. K_{ns} will therefore be denoted as K_s throughout this report.

2.4.1 Philip's Infiltration Model

Philip's infiltration model is a widely used experimental method that assumes the steady state infiltration rate relates directly to the permeability coefficient, A_p. Since the DRI has a falling water head the infiltration rate decreases as the level declines. Steady state is achieved when the water head pressure equals the negative matric forces in the soil at the end of measurement and K_s equals the infiltration rate (Soilmoisture Equipment Corp., 2009).

$$F(t) = St^{0.5} + A_p t$$

where $F(t)$ is cumulative infiltration, S is sorptivity, A_p is the permeability coefficient. The rate at which water infiltrates is then

$$f(t) = 0.5St^{-0.5} + A_p$$

where $f(t)$ is the infiltration rate. A_p becomes the dominant term as t increases. There are different suggestions on how A_p relates to K_s being a commonly used value $A_p/K_s = ⅔$ (Fodor et al., 2011)

2.4.2 Hazen Model and Beyer Model

Empirical models have been standard tools for site investigations due to their simplicity. K_s is related to soils pore structure which is a parameter difficult to measure. However, pore structure is intrinsically dependent on soil particle size distribution (PSD) therefore, many empirical models have emerged that estimates K_s from particle size distribution (PSD) data. To obtain a greater reliability in the prediction of K_s, a comparison was made with two empirical models; Hazen model and Beyer model that utilizes this relationship. Hazen model express hydraulic conductivity proportional to the squared grain size diameter at 10% passing. Beyer model take also the effect of particle size uniformity into consideration in its equation (Wang et al., 2017).

Hazen model: $$K = C_H \frac{g}{v} d_{10}^2$$

where g is gravitational acceleration (L/T^2), v=fluid kinematic viscosity (L^2/T), coefficient

$C_H = 6.54 \times 10^{-4}$ and $d_{10} =$ the diameter (L) at which 10% of the sample's mass is comprised of particles with a diameter less than this value.

Beyer model: $$K = C_B \frac{g}{v} log\left(\frac{500}{c_u}\right) d_{10}^2$$

where $C_u = d_{60}/d_{10}$ and coefficient $C_B = 6 \times 10^{-4}$.
(Wang et al., 2017)

However, empirical models estimate probabilities from observations based on laboratory analysis with a limited number of variables. A dimensional analysis of the relationship between hydraulic conductivity and PSD conducted by Wang et al. (2017) found that the Beyer model often overestimated its predictions of hydraulic conductivity of the tested samples. In their work, the Hazen model was found to give a good prediction for relatively high K_s. However, it underestimated most samples with $K_s < 3 \times 10^{-4}$ m/s.

2.5 Expected Hydraulic Conductivity for Alluvial Soils

Due to a complex sedimentary-forming process, the material distribution in alluvial fans are highly heterogeneous which implies that their hydraulic properties also display a high heterogeneity. Thus, generally it is difficult to characterise the spatial distribution of the hydraulic conductivity in alluvial soils (Zhu et al., 2017). Kirsch et al. (2009) states that K_s in an alluvial (sand-gravel) aquifer can range over four decades. This is further supported by Heinz et al. (2003), Houston (2002), Sakata et al. (2013), Zhu et al. (2017) Gómez et al. (2019) that estimated K_s in alluvial fans. In the compiled information (Table 1), it can be seen that K_s varies widely and have been found to have a wide range between 1.1×10^{-6} to 4.8×10^{-1} m/s (Table 1).

Table 1. Estimated hydraulic conductivity for alluvial fans in different soils.

Authors	Method	Zone characteristics	Hydraulic conductivity [m/s]
(Zhu et.al, 2017)	Kozeny–Carman equation. Empirical method that derives hydraulic conductivity from grain size and porosity	Coarse sediments	$> 3.47 \times 10^{-3}$
		Medium-coarse sediments	$3.47 \times 10^{-4} < K < 1.16 \times 10^{-3}$
		Fine sediment	$< 3.47 \times 10^{-4}$
(Houston, 2002)	Pumping test in boreholes	Sheetflood couplets of gravel-sand or gravel-clay	5.79×10^{-5}
(Sakata et al., 2013)	Pumping test in boreholes	Gravel deposit	$1 \times 10^{-5} - 1 \times 10^{-2}$
(Heinz et al., 2003)	Laboratory permeameter	Alternating gravel (glaciofluvial body)	$1.1 \times 10^{-6} - 4.8 \times 10^{-1}$
(Gómez et al., 2019)	Pumping test in boreholes	Unconsolidated quartenary aquifer (complex arrangement of clay, silt, sand and gravel)	$5.5 \times 10^{-5} - 2.9 \times 10^{-4}$

2.6 Hydrus – Modelling Software

Hydrus-1D is a free software used to model flow, heat and solute concentrations. It is a finite element model used in various saturated, porous media. It can thus be applied to estimate groundwater recharge (GWR). Hydrus-1D numerically solves a modified version of Richard's equation (Šimůnek et al., 2013).

Richard's equation:
$$\frac{\delta\theta}{\delta t} = \frac{\delta}{\delta z} \cdot \left[K(\theta) \cdot \left(\frac{\delta h}{\delta z} + 1 \right) \right] - S$$

where θ=volumetric soil water content (-), h=pressure head (L), t=time (T), z=vertical space coordinate, K=hydraulic conductivity (LT^{-1}) and S=optional sink term that accounts for root water uptake (T^{-1}).

Hydrus-1D offers several different models to solve unsaturated conductivity ($K(h)$) and soil water retention ($\theta(h)$). The chosen model in this study is the van Genuchten-Maulem water retention model because of its relative simplicity and performance. The model has a good fitting to experimental results for various K_s with an exception of very low conductivity soils ($< 9.5 \times 10^{-9}$ m/s) according to Genuchten van (1980). The soils tested in Chocaya basin all have a hydraulic conductivity well above 9.5×10^{-9} m/s indicating that the model is well suited.

Hydrus-1D offers ways of predicting soil hydraulic properties from textural properties of the soil. One of the two available methods, which is used in this report, is called the Rosetta module. The inputs used are the fraction of sand, silt and clay together with bulk density (ρ_b) and water content at 33 kPa (field capacity, Θ_{fc}) and 1500 kPa (wilting point, Θ_{wp}) respectively. Rosetta uses a large database to predict K_s and the van Genuchten-Maulem water retention parameters (saturated water content (Θ_s), residual water content (Θ_r), alpha (α), and n) with given inputs (Radcliffe et al., 2010). It is possible to interchange Θ_s and Θ_r with porosity (ϕ) (Stephens et al., 1998; Turesson, 2006) and wilting point (Θ_{wp}) (Genuchten van, 1980) respectively.

Hydrus-1D also offers an inverse optimization routine to estimate in situ soil hydraulic properties from measured time series of soil water content (θ). The inverse method combines forward soil water flow models (numerical solution of Richards's equation) and an algorithm for parameter estimations and is based on the minimization of an objective function describing the difference between observed and computed values. This routine can work as a practical and reliable methodology to obtain field-scale hydraulic characteristics. However, it is important to assess that the optimized parameters are physically realistic, as this decreases with an increased number of optimized parameters. (Ritter et al., 2003)

2.6.1 Evapotranspiration

The estimation of reference evapotranspiration (ET_0) in water cycle is important in near-surface environments. Hydrus-1D offers two equations for this; The Hargreaves equation (HG) is an empirical approximation requiring only air temperature data whereas the Penman-Monteith equation (PM) is a physically based approach where meteorological input data are air temperature, wind speed, relative humidity and solar radiation (Šimůnek et al., 2013). The use of Hargreaves equation (HG) is motivated when meteorological data is missing due to its simplicity and its approximation of ET_0 have been proven to be in reasonable agreement with the Penman-Monteith equation (PM) over long time steps (Droogers et al., 2002; Hargreaves, 1994). PM is more complicated and thus it can be difficult to obtain the required accuracy of the data. However, it is a well-documented method that have been implemented in a wide range of software and is proven to have a good performance in different climates. (Droogers et al., 2002)

3. Method

3.1 Electrical Resistivity Tomography (ERT)

A total of 11 ERT surveys were performed in the Chocaya basin (one survey at Location 5 and two at remaining locations (1, 2, 3, 4 and 6). The ERTs were carried out using an ABEM Terrameter LS 2 resistivity meter as seen in Figure 6. The used cables had 21 takeout's each and the electrodes were of stainless steel. The electrode array used in this study were Gradient array (Figure 4).

Figure 6. Pictures of the cable and steel electrodes (left) and ABM Terrameter LS 2 resistivity meter (right) used in the field work.

The depth of penetration and degree of resolution is based on the length of the cable layout and electrode configuration. The desired depth of penetration was around 1.5 meters and a high resolution was desired to obtain a more accurate model for the top soil layers. The profile length was 10 or 20 meters which comprised of one and two cables respectively. The numbers of electrodes used were 20 per cable which corresponds to an electrode spacing of 0.5 m.

The data inversion of apparent resistivity was performed using the software Res2Dinv. The same software was used to delete outliers in the data set that are caused by poor measurements. Res2Dinv generates a chosen number of iterations to lower the Mean Squared Error (MSE). Resulting inversions where graphically presented using Erigraph (Guidline Geo, 2007) and Eriviz (Guidline Geo, 2009).

3.2 Double Ring Infiltrometer (DRI)

A Double Ring Infiltrometer (DRI) was used for in situ measurements for estimating infiltration rates, I (m/s), of soils. The tests were conducted according to 2830K1 guidelines (Soilmoisture Equipment Corp., 2009). Both rings have a height of 0.3 m and diameters of 0.28 m (inner ring) and 0.52 m (outer ring) (Figure 5). The cylinders were inserted 0.05 m into the

ground and the bottom edges were sealed with clay to prevent leakage. The rings were filled up to an equal level. The outer ring was refilled sporadically to keep an equal level with the inner ring during infiltration. A Solinst absolute water level datalogger model 3001 (Solinst Canada Ltd, 2019) was used in the inner ring to measure the barometric pressure over time. The level datalogger measures both water and atmospheric pressure henceforth a barometrical compensation of the data is needed. This was achieved by simultaneous measurements of the changes in atmospheric pressure with a Solinst Barologger model 3001(Solinst Canada Ltd, 2019). The test continued until a constant infiltration rate was reached with additional refills at locations with higher infiltration rate. The accumulated infiltration data was fitted to the Philip's equation to obtain K_s. The parameters sorptivity (S) and the permeability coefficient (A_p) where optimized using least square method with data obtained from the two data loggers.

3.3 Soil Samples

Soil samples were taken at Location 1, 2 and 5. At Location 1 samples were obtained at the surface, and at depths of 0.6 m and 1.05 m. At Location 2 samples were collected at the surface and at 0.6 m. At Location 5 samples were collected from the river bed side at depths of 0.05 m, 2.6 m and 3.2 m, where different layers were visually observed (Figure 15). See Appendix A, Table A 1 for the coordinates corresponding to each location. Sampling was done both to correlate resistivity data with subsurface layers and to obtain physical soil properties. The particle size distribution (PSD) curves were obtained through sieving tests with the used sieve sizes presented in Appendix A, Table A 2. Clay, silt and sand were collected in the bottom pan and individual fractions determined through a hydrometer test (ASTM D422-63, 2007). The other physical properties determined in a laboratory were bulk density (ρ_b), field capacity (Θ_{fc}), wilting point (Θ_{wp}) and porosity (ϕ). These parameters are needed to estimate soil hydraulic parameters with the Rosetta module.

It should be noted that the sieves sizes used were the ones available at the host institution and not equivalent to the Swedish standard of sieve testing (SIS, 1992). The smallest sieve used was standard test sieve No. 8 with 2.36 mm openings. The percentage of sand, silt and clay that was conducted through the hydrometer test has an upper limit of 2 mm for sand. This means that there is a gap of 0.36 mm in the tests.

3.4 Precipitation and Soil Water Content (θ)

Precipitation and soil water content (θ) were measured at Location 1. An Onset rain gauge model RG3-M (Onset, 2020b) was installed to record precipitation and temperature data. Soil water content (θ) was measured and logged at 0.10, 0.45, 0.80 and 1.05 m depths using soil moisture sensors model S-SMC-M005 (Onset, 2020a), and a CR300 data logger (Campbell Scientific, 2020) (Figure 7). Measurements are taken every 5 minutes continuously. The equipment was installed 2019-10-17 and data was collected 2020-01-17. It is worth to mention that the equipment installed in this location is still measuring, and will be the basis for future hydrological studies in the Chocaya basin.

Figure 7. The assembled Onset rain gauge (left) and the installation process for the soil moisture sensors (right).

3.5 Model Setup

Hydrus-1D offer various settings and equations to estimate different features. This together with case specific input parameters is found in Appendix D. Those settings and assumptions of extra relevance for this report will be further explained and motivated below. The obtained information from ERT, PSDs and DRI tests were used in order to create infiltration models over Location 1 and the alluvial plain.

3.5.1 Main Processes and Geometry Information

The hydraulic model included water flow and discarded vapour flow. No root water uptake was incorporated in the model considering that the vegetation coverage on the plain was scarce.

Location 1 and the alluvial plain was modelled as 3 respective 4 layers between 0-5.0 m (Appendix C, Figure C 1). A depth of 5m was chosen as it is the approximate depth below surface where the deepest soil sample was taken. The surface at Location 5 is estimated to 1-2 m below remaining locations. The low number of layers in the columns of Location 1 and the plain is due to insufficient data of the stratigraphy. Thus, the models were built to be simple rather than too complex. A total of 4 observation nodes were added to the model at depths corresponding to the installed soil moisture sensors in order to facilitate comparison.

3.5.2 Sub Models

The hydraulic model was set to single porosity model (van Genuchten-Mualem model) under the assumption that there are no major differences in hydraulic permeability and that only mobile flow regions exist in the subsoil. Estimating net evapotranspiration (ET_0) offers two choices in Hydrus-1D, the Hargreaves equation and the Penman-Monteith equation (Šimůnek et al., 2013). Both methods were tested together with precipitation data to find the best suited model. The meteorological data was retrieved from the meteorological station Chaupisuyo situated 20km in east direction from Chocaya alluvial plane at a proximate elevation.

3.5.3 Boundary Conditions and Time Series

The top boundary condition was set to "atmospheric BC with surface layer" to allow the use of meteorological data as well as surface flooding in the model. The bottom boundary condition was set to "free drainage" due to the large distance between soil surface and groundwater table (approximately at 40 m below surface). The time series in the model was set to November 2018 - January 2020 in order to capture a part of the rainy season (November-April) in the region (Renner et al., 2000).

3.5.4 van Genuchten-Maulem Parameters

Various combinations of input parameters were tested in accordance to literature referenced in the 2.6 Hydrus section. Residual (Θ_r) and saturated water content (Θ_s) were both simulated by the Rosetta module and interchanged by wilting poing (Θ_{wp}) and porosity (ϕ) in different simulations. Remaining water retention curve parameters were all simulated by the Rosetta module. The pore-connectivity factor (l) was set to a standardised value of 0.5 (Mualem, 1976).

3.5.5 Calibration and Model Comparison

The parameters Θ_r, Θ_s, α, n, and K_s were calibrated for all three layers, at Location 1, using Hydrus' built in inverse parameter estimation. Measured soil water content (Θ) at depths of 0.10, 0.45, 0.8 and 1.05 m was used as input data for the inverse parameter estimation. The calibrated parameters were used to build a model for Site 2. An additional model was built using non-calibrated parameters from Philip's equation and the Rosetta module. This was done as part of a sensitivity analysis of the infiltration rate. The calibrated model was never validated due to the short range of soil moisture content data. R^2 and RMSE were chosen indicators to present the errors of the different models.

The coefficient of determination (R^2) is a statistical measure of how well the predicted values approximate the observed values where $R^2=1$ indicates that the regression predictions perfectly fit the observed values.

$$R^2 = \left(\frac{\sum_{i=1}^{n}(O_i - \bar{O})(P_i - \bar{P})}{\sqrt{\sum_{i=1}^{n}(O_i - \bar{O})^2} \sqrt{\sum_{i=1}^{n}(P_i - \bar{P})^2}} \right)^2$$

where O=measured soil water content (θ) and P=estimated soil water content.

Root Mean Square Error (RMSE) is the standard deviation of the residuals and indicates how close the observed values are to the model's predicted values. Lower RMSE indicate better fit.

$$RMSE = \left[\frac{1}{n} \sum_{i=1}^{n}(O_i - P_i)^2 \right]^{1/2}$$

where O=measured soil water content (θ), P=estimated soil water content and n=number of observations. (Feki et al., 2018)

4. Results

4.1 Electrical Resistivity Tomography (ERT)

The inverted ERT surveys all show a root mean square error (RMSE) lower than 10%. The number of iterations for each survey was set to 5. The calculated resistivity from ERT surveys predominately ranged from 200 – 2000 Ωm with certain spots reaching above and below that range which is in consistency with the findings of Gonzales Amaya et al. (2018) where the electrical resistivity in the unsaturated zone that consisted of boulders in matrix of fine material ranged from 200-1000 Ωm in Punata alluvial fan. Gómez et al. (2019) on the other hand found that the electrical resistivity in the unsaturated sediment in an alluvial fan in the central part of Bolivia ranged from 10-100 Ωm, however the sediment was clay abundant.

The legend of 100 – 5000 Ωm was chosen to obtain a good visual comparison from the majority of the subsurface soils. The depth of the profiles is 1 meter for all locations except at Location 5 where the profile depth was 4 m. It should be noted that the darkest red colour represents very high resistivities (>5000 Ω) at Location 5 (Figure 9). Location 1 and 2 (Figure 8) show tendency of layering in the soil at approximately 0.4m (marked with black dotted lines in the figure) with lower resistivity at the top and higher in the bottom layer.

Figure 8. 3D-view of ERT results for Location 1 (left) and Location 2 (right) with an electrical resistivity range of 100 – 5000 ohm-m. Profile depth is 1 m.

Location 3, 4 (Figure 9) and 6 (Figure 10) present more heterogeneity in the resistivity results. Location 4 has overall slightly higher values than Location 3 and 6. There is a visual spot of lower resistivity in the centre of the ERT measurements in Location 3, 4 and 6. Location 5 (Figure 10) displays a slight tendency of layering with low resistivity at the top (0-1m), higher resistivity in the middle (1-3 m) and then again a layer with lower resistivity between 3-4 m depth (marked with black dotted lines in the figure).
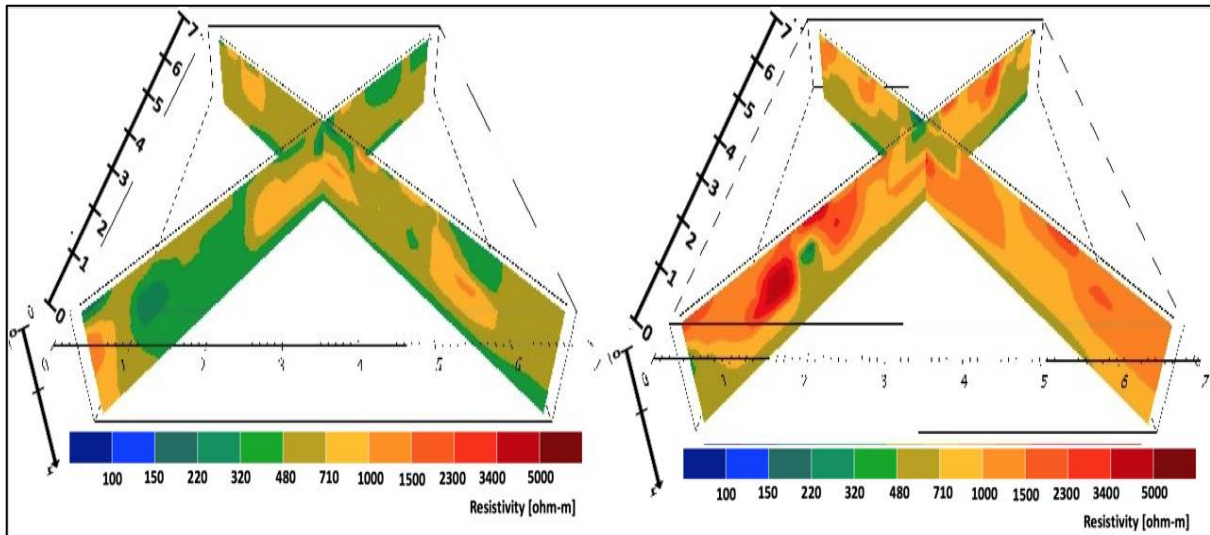
Figure 9. 3D-view of ERT results for Location 3 (left) and Location 4 (right) with an electrical resistivity range of 100 - 5000 ohm-m. Profile depth is 1 m.
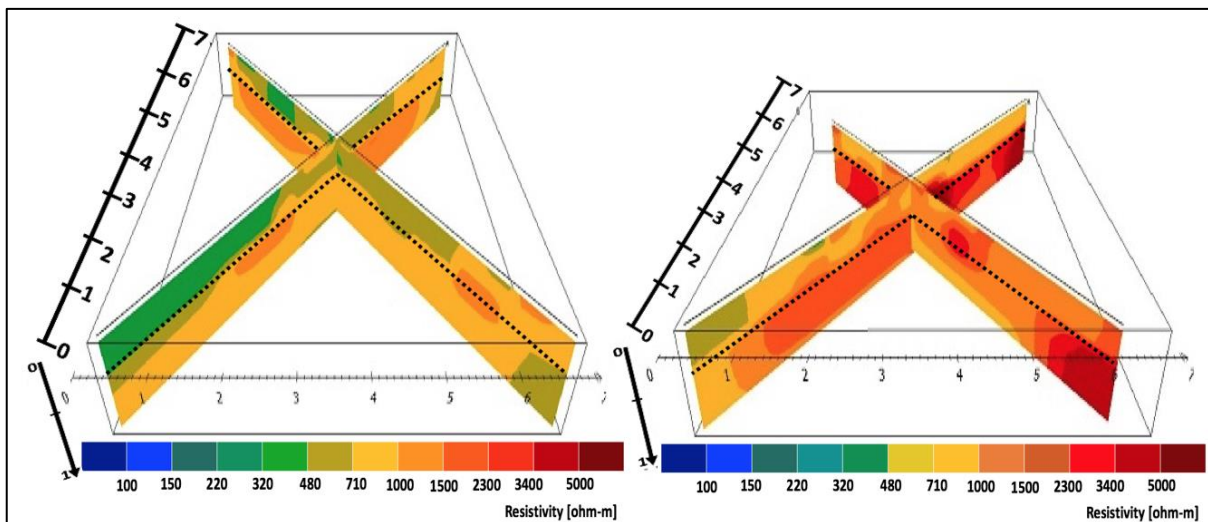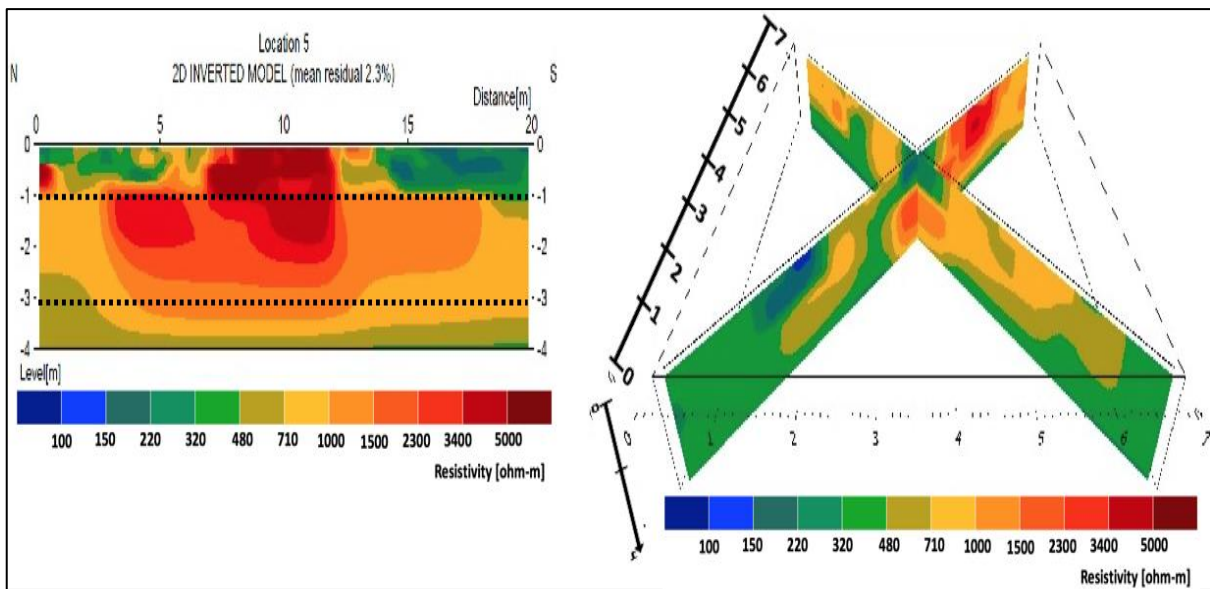

Figure 10. 3D-view of ERT results for Location 5 (left) and Location 6 (right) with an electrical resistivity range of 100 - 5000 ohm-m. Profile depth is 4 m for Location 5 and 1 m for Location 6.

4.2 Double Ring Infiltrometer (DRI)

The infiltration process at Location 1, 2, 4 and 6 are presented in Figure 11. The peaks represent refills of the DRI cylinders. Location 1 (0.6 m) and 6 (surface) were not refilled due to a slow infiltration. The depth shown has as reference the position of the level logger. The infiltration velocity is generally faster at the start before gradually decreasing to a constant value. This is when the soil is saturated and steady-state is reached.
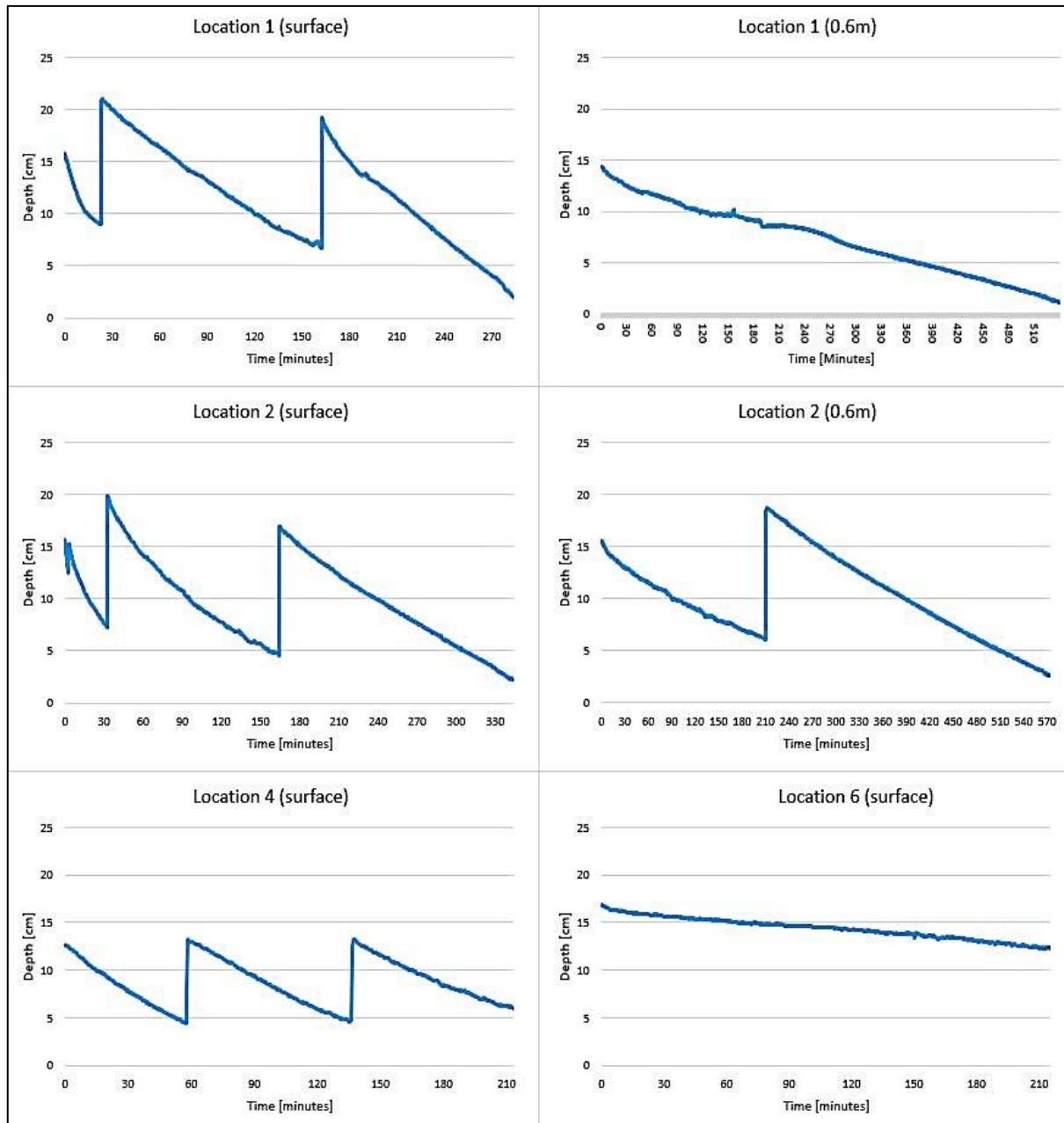
Figure 11. Infiltration processes at different depths at Location 1, 2, 4 and 6.

The infiltration rate is shown in Table 2 and varies between 1.4E-05 – 1.8E-06 m/s with Location 1 (0 m) displaying the highest infiltration rate and Location 6 (0 m) the lowest.

17

Table 2. The infiltration rate (m/s) from the double ring infiltrometer test at Locations 1, 2, 4 and 6.

Location	Depth [m]	Infiltration rate [m/s]
1	0	1.4×10^{-5}
1	0.6	2.5×10^{-6}
2	0	1.0×10^{-5}
2	0.6	3.3×10^{-6}
4	0	1.1×10^{-5}
6	0	1.8×10^{-6}

The infiltrated depth (Figure 12) show one infiltration curve for each location and depth respectively that resolved in the lowest RMSE fit to the Philip's equation. All figures show a good fit with a low RMSE. The time span of which the infiltration tests were conducted differ depending on the infiltration rate at the specific location. It can be observed from the figures that a lower infiltration rate also generates a lower K_s.
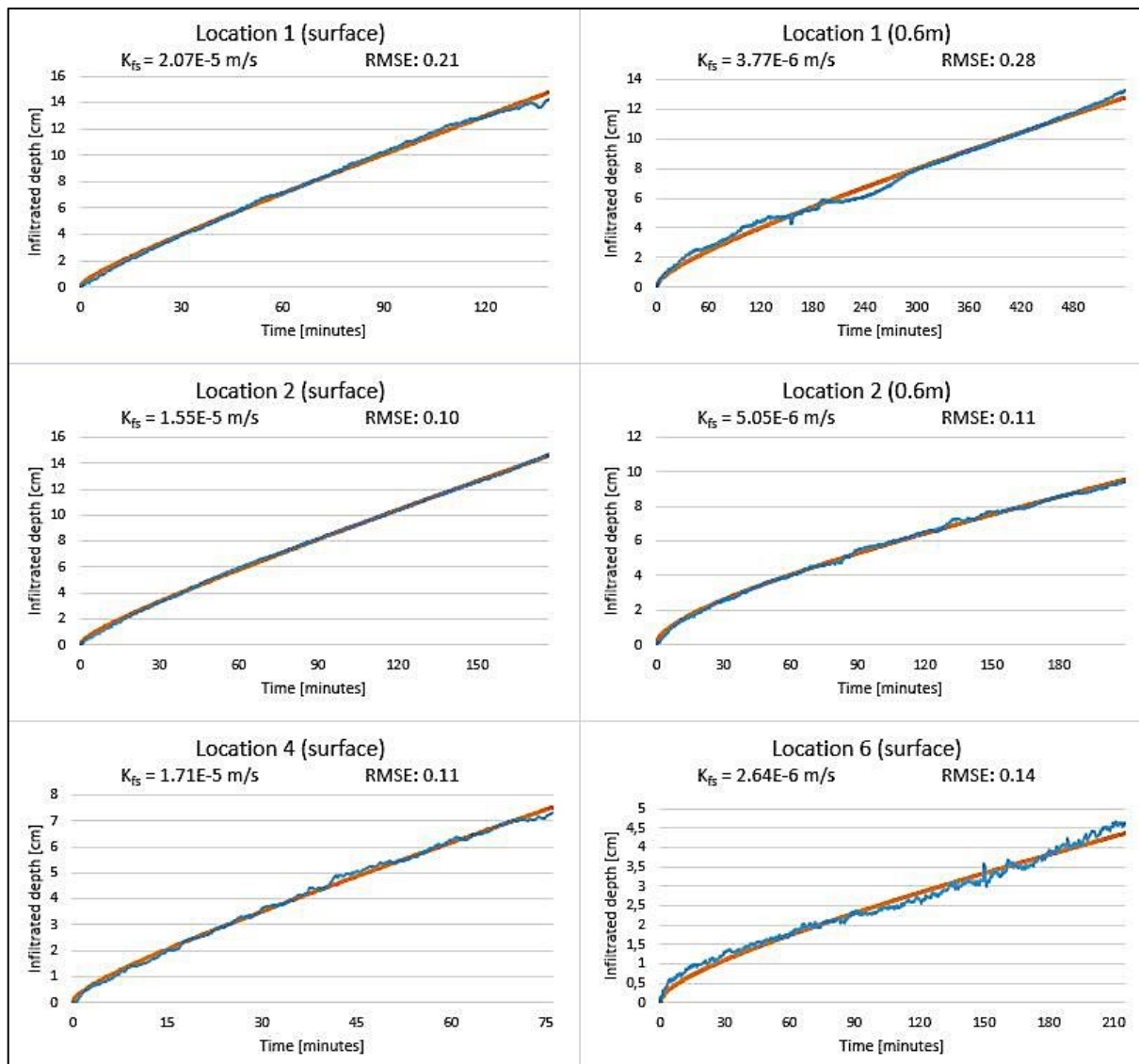
Figure 12. Infiltrated depth at Location 1, 2, 4 and 6 with the lowest achieved RMSE.

4.3 Particle Size Distribution (PSD)

The PSD curves at different depths from Location 1, 2 and 5 are visualized in Figure 13. A result from the laboratory analysis are seen in Appendix A, Table A 2. PSD curves for Location 1 (top) and 2 (middle) show resemblances with 20-45 % of the particles < 1 mm. Location 1 displays an increase in coarse material with depth. Location 2 instead displays an increase in fine material with depth.
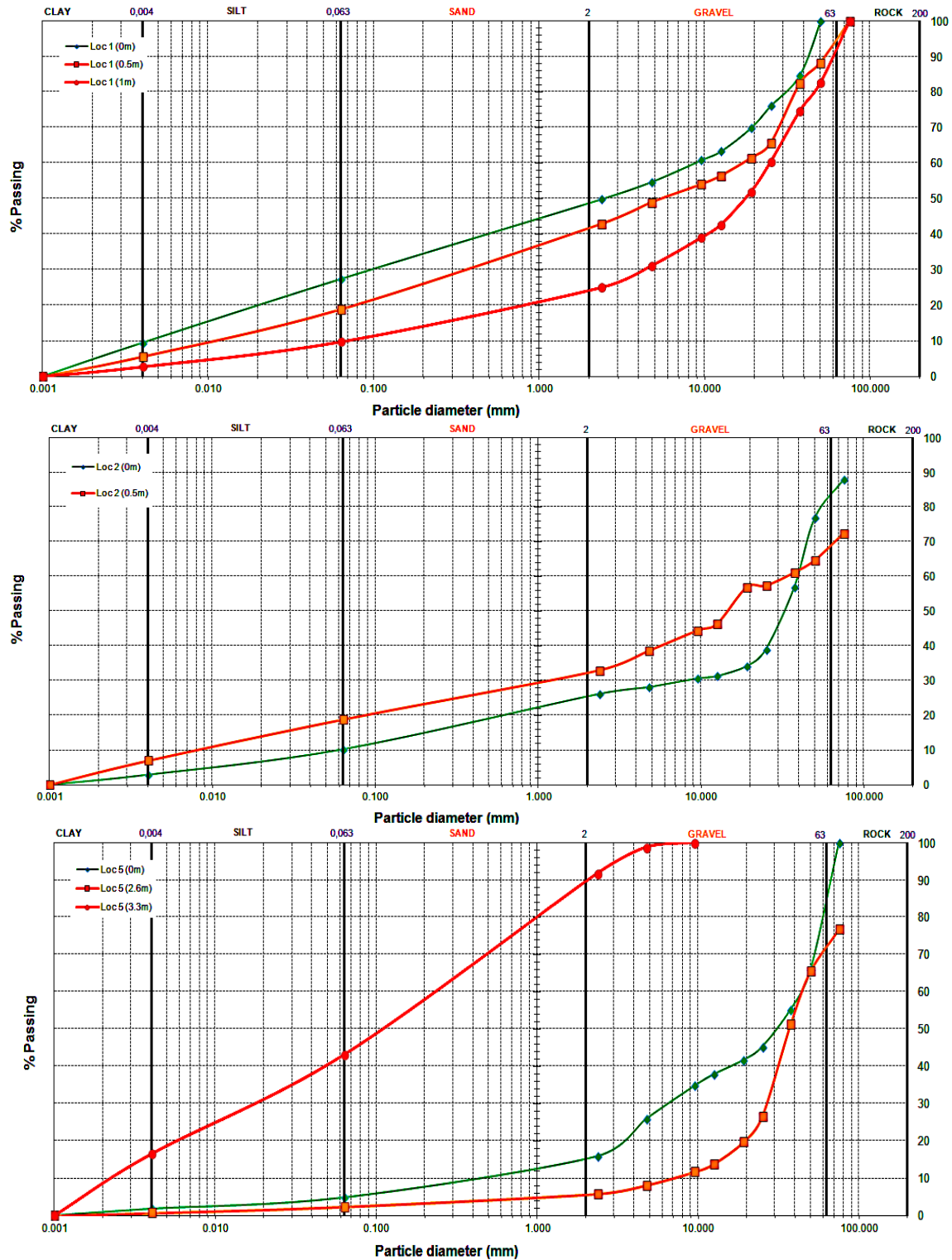
Figure 13. Particle size distribution curves for different depth at Location 1 (top), Location 2 (middle) and Location 5 (bottom).

The upper and middle layer in Location 5 were composed of more coarse materials 5-12 % < 1 mm. The lowermost layer is displaying higher percentage of fine-grained material and the middle layer the lowest percentage. Figure 14 displays the compiled PDSs for Location 1, 2 and 5 with the general trend that Location 5 showed largest number of both fine particles (3.3 m) and coarse material (2.6 m and 0.05 m) whereas PSDs for Location 1 and 2 are found in between those.
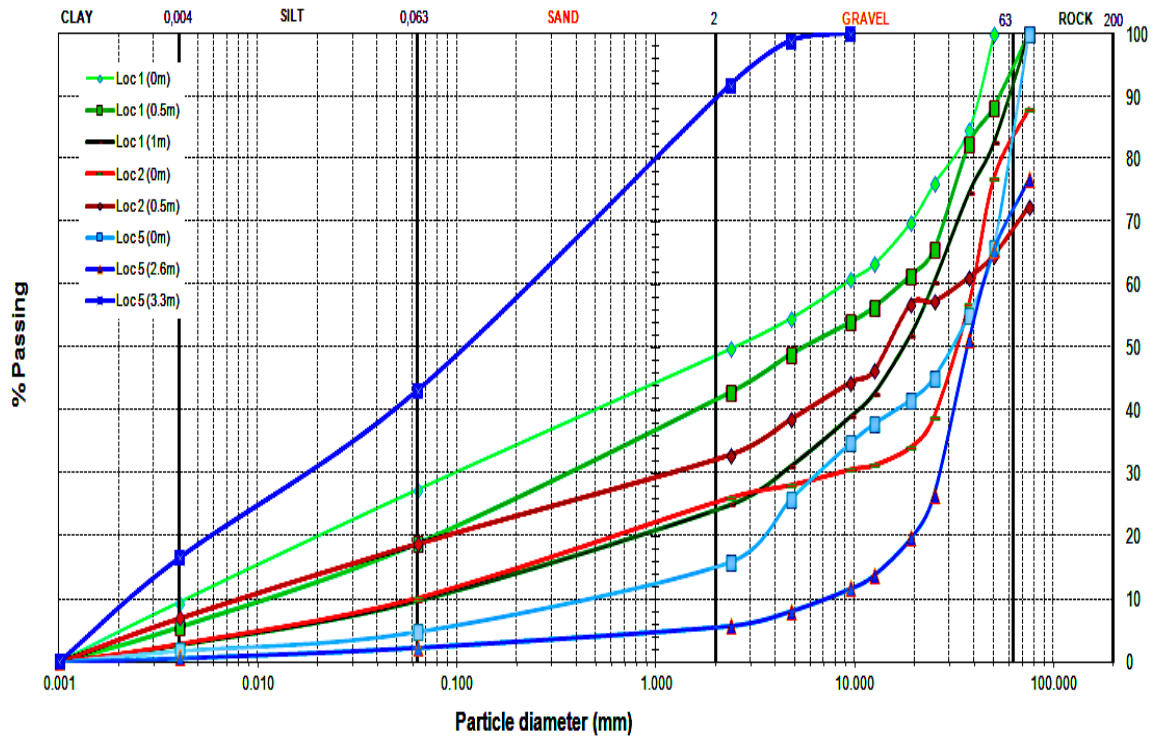
Figure 14. Particle size distributions for Location 1 (green), Location 2 (red) and Location 5 (blue).

The notable stratigraphy (1-4 m) in the riverbed (Location 5) distinguish three soil layers (Figure 15). The colored arrows (green, orange and red) in the figure represent the three corresponding PSDs from the site (Figure 13, bottom). Visually the middle layer (orange) shows more coarse material whereas the bottom layer (red) much more fine material. This coincided with the measured electrical resistivity that were higher at 2.6 m depth and lower at 3.3 m depth (Figure 9), K_s that were highest at 2.6 m depth and lowest at 3.3 m depth (Table 3) and proportion fine grained material that were highest at 3.3 m depth and lowest at 2.6 m depth (Figure 13). The red box represents the center of the ERT measurements from Location 5 (Figure 9).
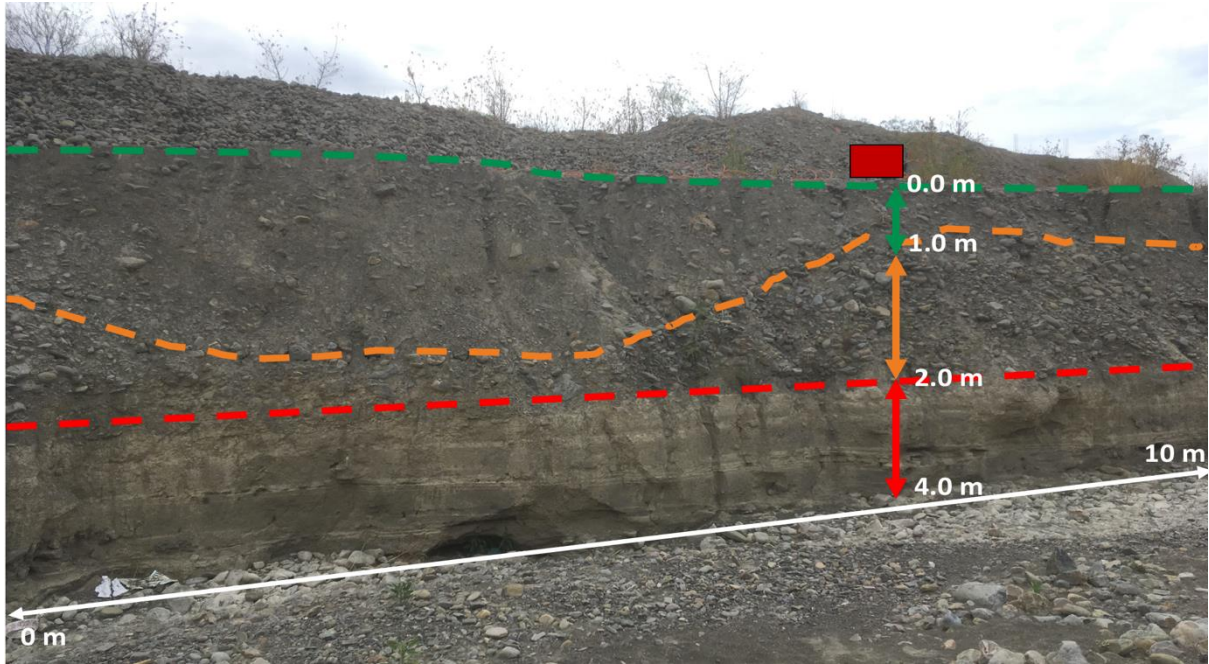
Figure 15. Stratigraphy in a riverbed in the Chocaya alluvial fan (Location 5). The soil profile displays three different soils visually determined marked with dotted lines. The red box represents the center of the ERT measurement.

4.4 Hydraulic Conductivity

The hydraulic conductivity results are compiled in Table 3. K_s decreases with depth at Location 1 for Philip's equation. Location 1 indicated highest K_s at 1.05 m depth and lowest at 0.6 m for Hazen and Rosetta. K_s increased with depth at Location 2 for Philip's, Hazen and Rosetta. K_s for Location 5 showed highest values for the middle layer (2.6 m) and lowest for the bottom layer (3.3 m) for both Hazen and Rosetta. However, Hazen equation gave much higher K_s for the top (0.05 m) and middle layer and much lower for the bottom layer.

Table 3. Calculated hydraulic conductivity (K_s) for Philip's equation, Hazen equation, Beyer equation and the Rosetta module.

| Location	Depth	Philip's [m/s] (RMSE)	Hazen [m/s]	Beyer [m/s]	Rosetta [m/s]
1	0	2.1×10^{-5} (0.21)	1.6×10^{-7}	-8.2×10^{-8}	6.6×10^{-6}
1	0.6	3.9×10^{-6} (0.28)	5.2×10^{-7}	-2.7×10^{-7}	4.2×10^{-6}
1	1.0	-	2.3×10^{-5}	1.7×10^{-6}	1.5×10^{-5}
2	0	1.6×10^{-5} (0.10)	2.3×10^{-5}	-2.2×10^{-6}	2.1×10^{-5}
2	0.6	5.1×10^{-6} (0.11)	6.4×10^{-7}	-5.2×10^{-7}	4.3×10^{-6}
4	0	1.7×10^{-5} (0.11)	-	-	-
5	0	-	7.8×10^{-4}	4.4×10^{-4}	4.9×10^{-6}
5	2.6	-	2.3×10^{-1}	3.9×10^{-1}	5.4×10^{-6}
5	3.3	-	3.4×10^{-8}	2.4×10^{-8}	3.8×10^{-6}
6	0	2.6×10^{-6} (0.14)	-	-	-

A comparison of calculated K_s between the four equations showed that Philip's equation and Rosetta gave similar values for the different locations. The calculated K_s for Philip's equation range between $2.6\times10^{-6} – 2.1\times10^{-5}$ m/s, the Rosetta module similarly predicted K_s over two decades between $3.9\times10^{-6} – 2.1\times10^{-5}$ m/s which coincide with expected hydraulic conductivity in alluvium (Table 1). Hazen equation gave similar values for Location 1 and 2 as Philip's and

Rosetta. The empirical methods using Hazen and Beyer equations respectively present a wide range of results, $3.4 \times 10^{-8} - 2.3 \times 10^{-1}$ m/s, especially for Location 5. 4 soil samples resulted in negative K_s (marked with red) using Beyer method which is physically impossible.

The empty cells for Philip's equation at Location 1 (depth 1 m) and at Location 5 (all depths) is because no DRI measurements were performed here. At Location 4 and 6 no soil samples were taken henceforth no hydraulic conductivities from Hazen equation, Beyer equation and the Rosetta module were achieved.

4.5 Hydrus-1D

Hydrus-1D models were created for Location 1 and the alluvial plain. The physical properties used as general input data for both models are found in Appendix D and the layer-specific input parameters are shown in Appendix C, Table C 1 & Table C 2.

4.5.1 Location 1

Two of the available equations to estimate evaporation where compared to choose the most well suited. The measured and simulated soil water content (θ) using both Hargreaves equation and Penman-Monteith equation can be seen in Figure 16. The different figures represent the 4 soil moisture sensors and its corresponding nodes in the model. Hargreaves equation captures the behavior of the measured θ to a greater extent for all the depths. Therefore, it was the chosen equation to estimate evaporation for continued simulations of the alluvial plain. The measured θ showed highest fluctuation in the top node (0.1 m) where θ ranged between $0.1 - 0.33$ for the period. The bottom node (1.05 m) showed least fluctuation with θ ranging between $0.14 - 0.22$ for the same period.
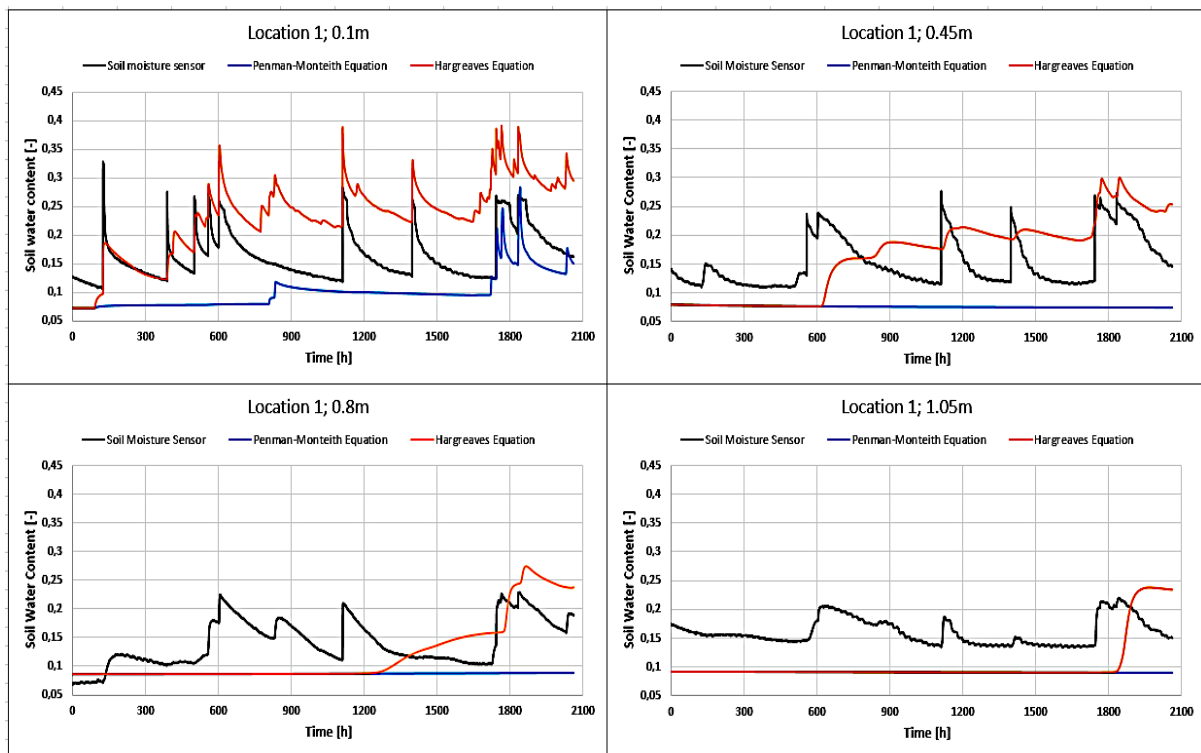

Figure 16. Measured soil water content (θ) (black) and simulated θ using Hargreaves equation (orange) and Penman-Monteith equation (blue) at Location 1, depth 0.1 m (top-left), 0.45 m (top-right), 0.8 m (bottom-left) and 1.05 m (bottom-right).

22

A comparison of θ and hydraulic conductivity K_s obtained from Philip's equation, Hazen equation and the Rosetta module can be seen in Figure 17. The simulated water content using K_s from DRI and Rosetta were similar and captured the general trend of measured θ well. However, the simulations didn't manage to capture the peaks in the middle of the period at depth 0.45 m and 0.8 m. Overall, they tended to underestimate the decrease in θ between rain events. The simulated θ using K_s from Hazen equation roughly captures the behaviour of the measured θ at 0.1 m. Model accuracy decreased with depth and did not capture the variations at 0.45, 0.8 and 1.05 m. Therefore, when further building the model for the plain, K_s values from Hazen equation was discarded.
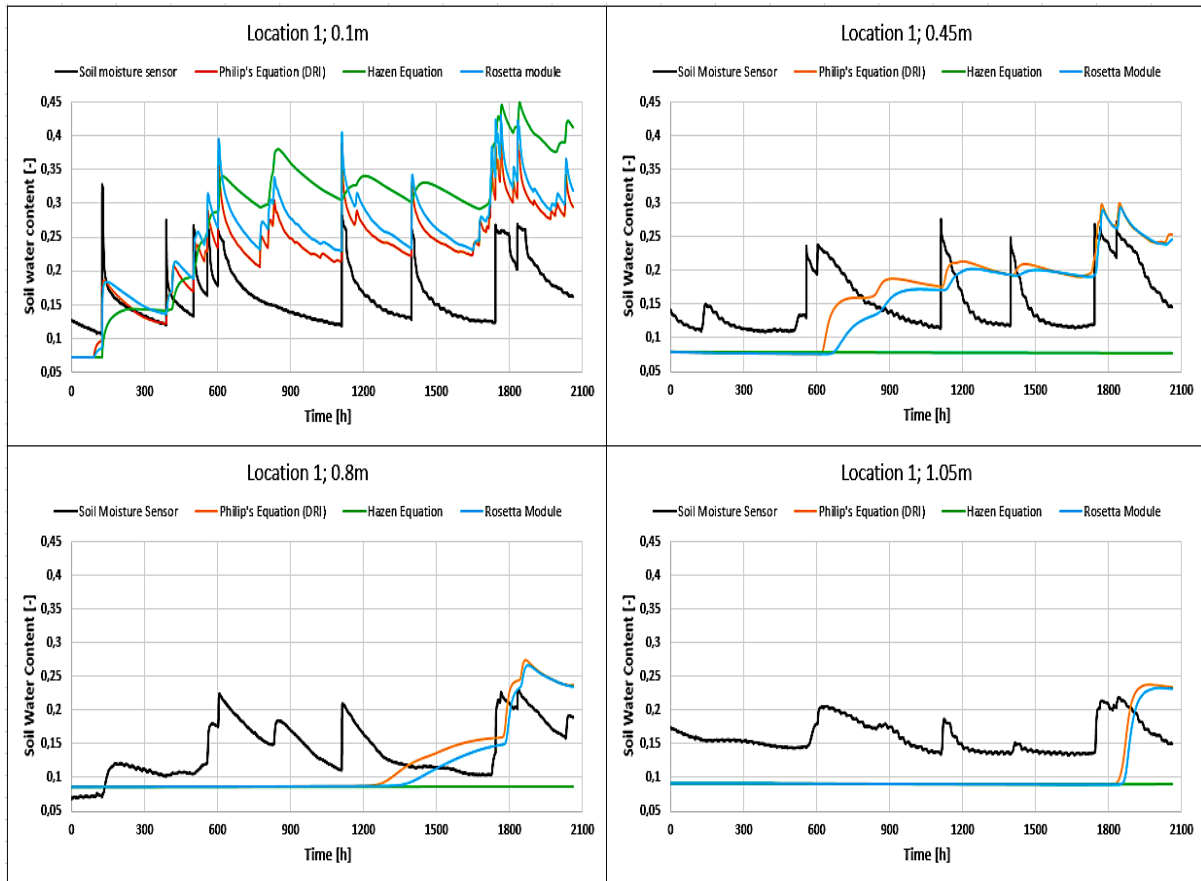
Figure 17. Measured soil water content (θ) (black) and simulated θ with K_s from Philip's equation (red), Hazen equation (green) and Rosetta module (blue) at Location 1. Depths: 0.1 m (top-left), 0.45 m (top-right), 0.8 m (bottom-left) and 1.05 m (bottom-right).

A comparison between two Hargreaves models using calibrated soil parameters from the inverse optimization and obtained values from DRI and Rosetta can be seen in Figure 18 (the result for 0.45 and 0.8 m are seen in Appendix B, Figure B 2). The inversed optimization model succeeded to capture the general patterns of θ and achieved a better fit for both 0.1, 0.8 and 1.05 m depths. However, the peaks succeeded by rain events are not captured well at 0.1 m. RMSE and R^2 was calculated for both models at all four observation nodes (Table 4). RMSE was lower for the inversion models and R^2 was higher with values between $0.36 - 0.82$.

23
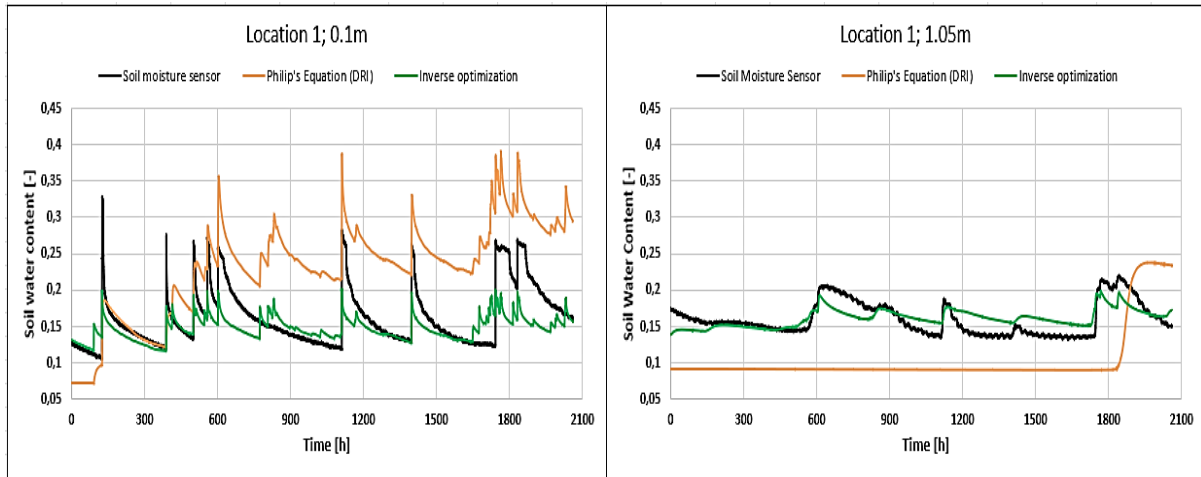
Figure 18. Measured soil water content (θ) (black) compared to the model using soil parameters from DRI (orange) and inverse optimization (green) respectively. Depths: 0.1 m (left) and 1.05 m (right).

Table 4. RMSE and R² for the field data model (DRI and Rosetta) and the inverse optimization model for all four nodes at depth 0.1, 0.45, 0.8 and 1.05 m.

RMSE [-]				
Model	*0.1 m*	*0.45 m*	*0.8 m*	*1.05 m*
Field data model	0.087	0.061	0.057	0.073
Inverse optimization	0.034	0.040	0.031	0.018
R²				
Model	*0.1 m*	*0.45 m*	*0.8 m*	*1.05 m*
Field data model	0.37	0.22	0.18	0.001
Inverse optimization	0.38	0.49	0.82	0.36

4.5.2 Alluvial Plain

The simulated models (Figure 19 and Figure 20) presents θ through the profile at specific observation time steps. The time steps are evenly divided along the simulated time every second month. The meteorological data was taken from the meteorological station Chaupisuyo and ranges between 19th of November 2018 to 9th of January 2020. This covers a complete rain season 2018-2019, a dry season 2019 and the start of the rain season 2019-2020.

Initial soil water content (θ_i) was estimated from the lab analysis where available water ranged between roughly 0.06-0.09. However, the samples were not stored in sealed containers and it can thus be assumed that θ is higher. It is also unknown what the soil water content was below 1 m. Therefore, separate models were built with an initial θ_i =0.1 and a gradual increase of θ_i = 0.1-0.2 respectively. To clarify, a total of 4 models were built which are presented in Table 5.

Table 5: A summary of differences between the 4 models built for estimating the infiltration rate in the alluvial plain.

Name	Parameters and soil characteristics taken from:	Initial soil water content [θ_i]
Field Model 1 (FM1)	DRI and the Rosetta module	0.1
Field Model 2 (FM2)	DRI and the Rosetta module	0.1-0.2
Inverse Model 1 (IM1)	Inverse optimization	0.1
Inverse Model 2 (IM2)	Inverse optimization	0.1-0.2

In FM1 and IM1 (Figure 19) it can be observed that the water fluxes in the top layers are mostly occurring during wet season but evens out over the year further down the column. However, both models result in no bottom flux during the simulated period. FM1 displays higher θ in the top layer (0-0.4 m) while IM1 shows a more even distribution of θ that also reaches further down the profile.

T0, T1, T2, T3, T4, T5 and T6 represents time steps evenly divided along the simulation period Nov, 2018 - Jan, 2020. The time steps are two months apart with T0 as starting time, T1 after two month from starting time, T2 after four months etc.
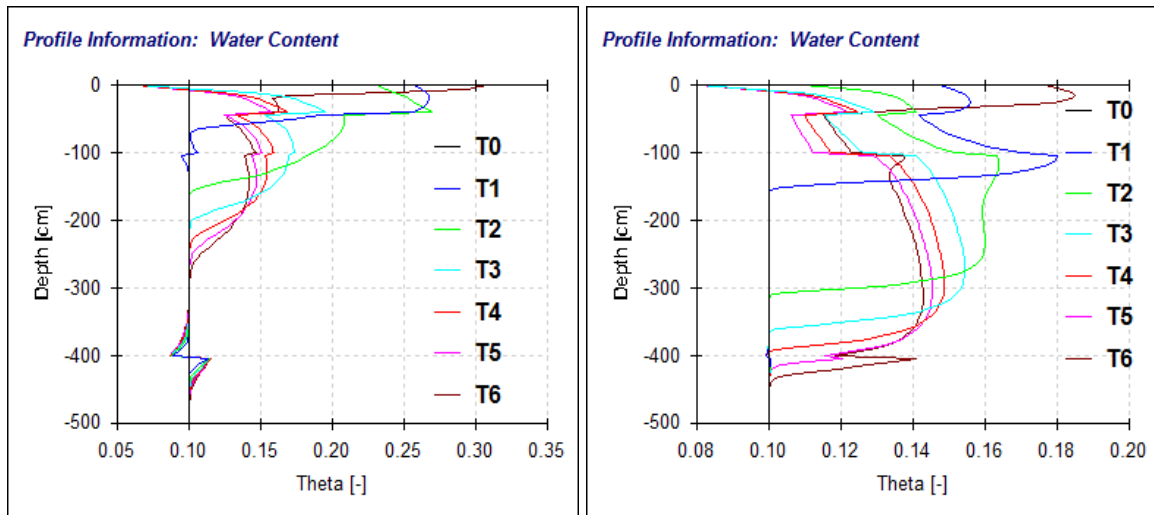
Figure 19. Simulated θ for the two models; Field model 1, FM1 (left) and inverse model 1, IM1 (right) using θ$_i$=0.1 throughout the profile. The simulation period is Nov, 2018 - Jan, 2020. Theta [-] is soil water content.

The results of FM2 and IM2 are presented in Figure 20. Model FM2 displays an increase in water content at the bottom of the profile already after the second time step (after four months). Both models show a rapid increase in θ between material 3 and 4. FM2 displays a higher θ in the top layer (0 - 0.4 m) but IM2 displays higher θ in the bottom layer (4.0 - 5.0 m).
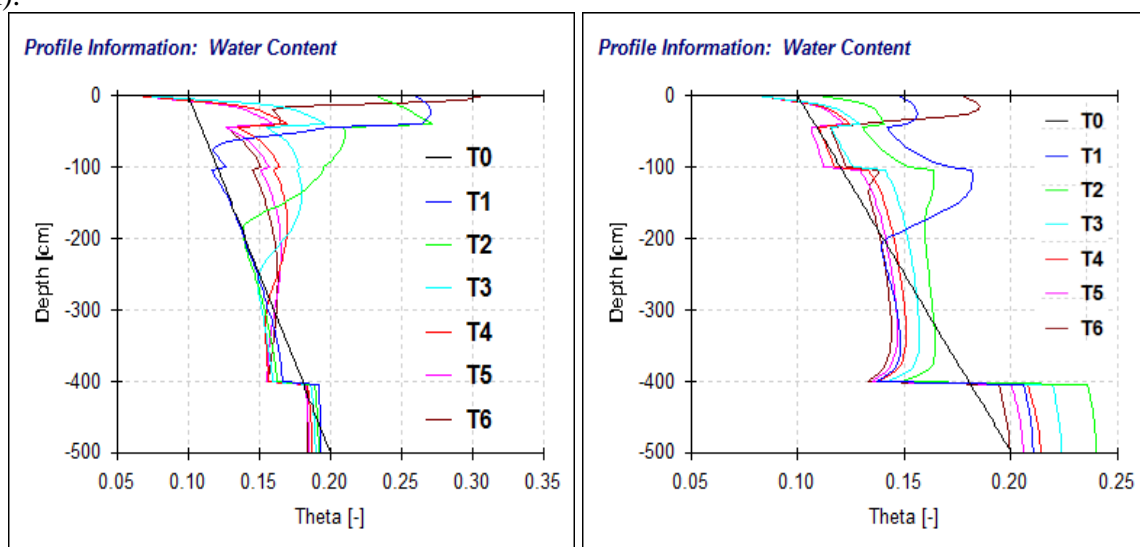
Figure 20. Simulated θ for the two models; Field model 2, FM2 (left) and inverse model 2, IM2 (right) using θ$_i$ = 0.1-0.2 (gradual) throughout the profile. The simulation period is Nov, 2018 - Jan, 2020. Theta is soil water content (-).

The cumulated bottom flux is after a year (8760 h) approximately 3.6 cm/year respectively 15 cm/year from the 5 m deep column for FM2 and IM2 (Figure 21). IM2 showed higher bottom flux after the simulated period. FM2 showed a nearly linear bottom flux. The soil water content in 5 nodes introduced along the depth of the soil profile can be seen in Appendix E, Figure E 2.
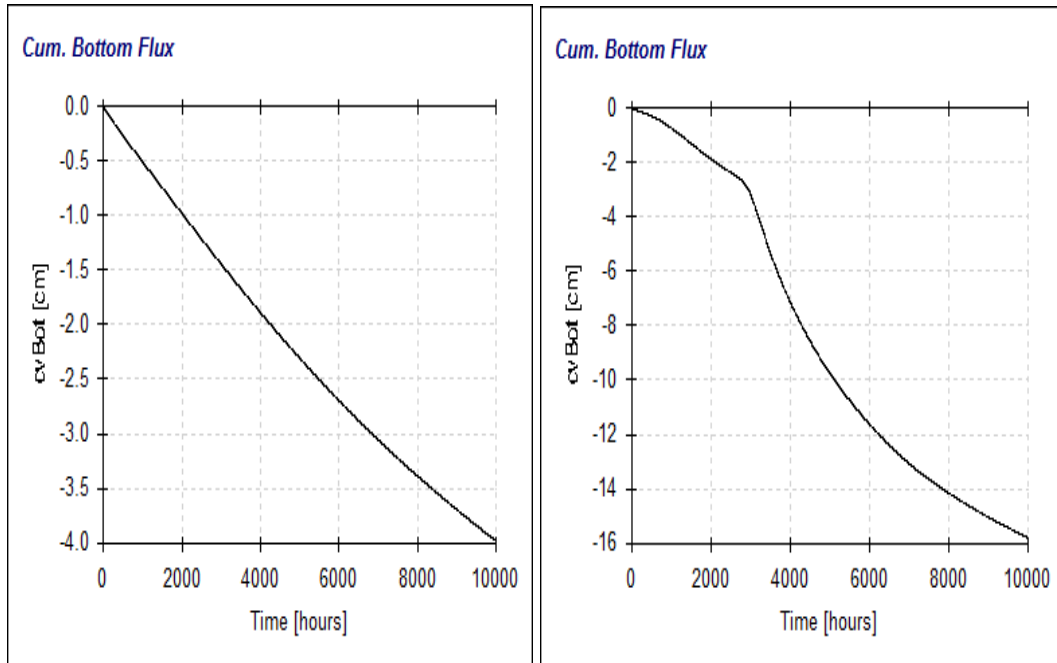
Figure 21. Simulated cumulative bottom flux at 5m for FM2 (left) and IM2 (right) in the alluvial plain for Nov, 2018 – Jan, 2020. Negative values indicate downward flux.

26

5. Discussion

5.1 Electrical Resistivity Tomography (ERT)

The electrical resistivity tomography (ERT) measurements that were used to assess the subsoil structures can potentially reduce soil sampling uncertainties. There is a good agreement between the perpendicular profiles (Figure 8 and Figure 9), hence the ERT surveys were retrieving consistent data. However, the optimal performance of ERT measurements in a coarse alluvial soil can be difficult to achieve as there is a possibility that the coarse soil structure might interfere with obtaining good electrode contact with the soil. An example is observed at Location 5 (Figure 9) where high electrical resistivity values were obtained, possibly caused by poor electrode contact. The apparent area of lower resistivity by the centre at Location 3, 4 and 6 (Figure 9) is possibly caused by residual clay that was used to prevent leakage during the DRI-tests.

The electrical resistivity cannot in solitary be interpreted as geological units (Bing, 2019). Therefore, ERT measurements and soil samples from Location 5 were used as an attempt to interpret the soil lithology. Figure 9 display layering tendencies which are further confirmed with the visual inspection (Figure 15). However, the interpretation became to some extent difficult due to bad electrode connection at the location ensuing misleading electrical resistivity data.

There is some research available that locally correlates electrical resistivity and saturated hydraulic conductivity (Kirsch et al., 2009). It is however not possible to get more than indications when implementing these correlations at the investigated locations. A working method for comparing these two instances would be beneficial since it would be a timesaving and simplifying way of improving hydrogeological modelling over large areas and depth with a variable landscape.

5.2 Hydraulic Conductivity (K_s) and Double Ring Infiltrometer (DRI)

The benefits of retrieving K_s from in situ measurements is that the created model is supposed to represent Chocaya basin. Another advantage is that DRI tests can obtain results from undisturbed soil whereas lab analysis result in a disturbed soil. There are, yet, potential errors with field measurements. During the DRI tests it is assumed that the amount of lateral flow is negligible, but if the inner and outer rings are not kept at an equal level it is likely that water will flow between them. It is possible that some of the noise in the infiltration curves are caused when refilling the outer ring resulting in fluxes between the two rings. The infiltration curves are expected to have been smoother without constantly refilling the outer ring but that would likely increase the infiltration trend line and thus overestimating K_s. No consideration has been taken to evaporation during the infiltration tests. This could have caused a small overestimation of the infiltration rate. A possible solution to prevent evaporation would be to place a lid on the inner ring. All DRI test reached constant infiltration from visually observing the graphs (Figure 11) and it can then be assumed that the test was long enough to obtain K_s.

5.3 Hydraulic Conductivity and Particle Size Distribution (PSD)

K_s (Philip's equation (DRI), Hazen equation and Rosetta) decreased with depth at Location 2 which consistent with the PSD curve that displayed a higher percentage of fine-grained material at depth 0.6 m. However, at Location 1 it was found that K_s (DRI) also decreased with depth

but here instead the PSD curve showed a larger amount of finer material at the top. One possible explanation for a higher K_s in combination with a lager fraction of finer sediments could be that the soil is dry leading to cracks in the fine-grained material.

K_s values obtained from Beyer and Hazen equations had larger spread than K_s obtained from DRI tests. K_s obtained from Hazen equation are lower in comparison to K_s from DRI and Rosetta, except for in Location 5 at depths 0.5 m and 2.6 m. According to Wang et al. (2017), Hazen equation has the potential of underestimating samples with $K < 3 \times 10^{-4}$ m/s which could explain this tendency. Both Hazen and Beyer equations are empirical equations based on the PSD curves. Resulting K_s change drastically from small changes in d_{10} and d_{60}. This implies that the sieving test must be well conducted with large enough samples to minimise errors. It would also be of interest to do several sieve tests with the same sample to assure correct results. The volume of the soil samples used in sieve tests conducted for this report were relatively small considering that the soils are containing boulders >100 mm in diameter together with a lot of fine sediments. It is therefore likely that the sieve test results are largely affected by how the samples were collected and non-accurate since boulders are not included in the diagram. Beyer equation gave four negative values for K_s which is physically impossible. Hence, the soil samples did not meet the empirical conditions for the model and it stresses the importance of using physical parameters when modelling the specific region. Therefore, the model with K_s from DRI should provide more reliable values in this situation. The benefits of using empirical equations such as Hazen and Beyer methods is that they provide simple models where you can retrieve an indication of K_s over large areas. Especially in areas with homogeneous soils without stones and blocks.

5.4 Hydrus-1D

Location 1 was modelled as three layers according to the information obtained from the ERT results (Figure 8). A tendency of layering in the soil at ~ 0.4 m depth are visible together with field observations of a soil structure change again at 0.8 m which is supported by the PSD curves (Figure 13). The bottom layer was only introduced as a buffer to prevent the model from crashing. Location 3, 4 and 6 exhibit stratified homogenous soil according to the ERT measurements with an identified layer starting around 1 m depth (Figure 9) and with similar electrical resistivity and K_s as Location 1 and 2. Therefore, the two simulation models created for Location 1 were additionally used as models designed for the alluvial plain. It can be observed that there is a delay of modeled soil moisture content compared to the measured values in Figure 17 and Figure 18. A possible explanation for this is that the soil at the locations of soil moisture sensors is disturbed. Thus resulting in a higher infiltration rate in the more porous soil.

The chosen model for meteorological data was the simpler Hargreaves equation in favour of the Penman-Monteith equation because of the better results in the calibration process (Figure 16). Hargreaves only accounts for Latitude and temperature to estimate variations in evaporation, whilst Penman-Monteith includes altitude, solar radiation, radiation parameters, sunshine hours, humidity and wind speed. Even though this data was collected at the nearby location Chaupisuyo it is possible that the model became too complex with added uncertainties using Penman-Monteith.

Using the Rosetta module offers a simple and relatively quick way of predicting soil hydraulic properties. If comparing K_s generated by the DRI and Philip's equation to K_s predicted by Rosetta it is observed that they show similar values and trends at Location 2 (Table 3). At Location 1 they present opposite trends to the level at which the highest and lowest K_s are

found. This indicates that the Rosetta module can be a useful tool, but the results should at the same time be treated with care.

The 4 models built for the plain (FM1, FM2, IM1 and IM2) have a fourth layer introduced. A bottom layer using soil parameters from Location 5 (3.3 m). This layer showed largest amount of fine material (Figure 15) and lowest K_s from the Rosetta module. It was assumed that similar layer deposits are present in the entire alluvial plain, hence this layer could potentially exhibit slow infiltration rate, thus being significant for the infiltration capacity of the soil. However. IM1 and IM2 that uses parameters from inverse optimization obtained K_s lower than the lowest value obtained from the Rosetta module. This raises suspicions that either the inverse optimization or the Rosetta module generated misleading results. One advantage with an inverse optimization method is that hydraulic parameters are estimated directly from measured data. However, the obtained parameters must be ensured to be physically realistic and representative of the in-situ study. This was done by comparing them to the parameters obtained in situ (K_s), in laboratory (Θ_{wp} and ϕ) and by Rosetta (K_s, Θ_r, Θ_s, *alpha* and *n*). slow infiltration

The findings of FM1, FM2, IM1 and IM2 were that the initial soil moisture content (θ_i) of the layers has a large impact on the resulting bottom flux. According to the simulation results, there is no bottom flux when $\theta_i =0.1$. However, it becomes prominent when θ_i is increased through the column and water reaches the bottom already after two months for both FM2 and IM2. The cumulative bottom flux after a year became approximately 3.6 cm/year and 15cm/year for FM2 and IM2 respectively. This implies the importance of measuring θ at several depths prior to running the model. However, it is still unlikely that rainwater infiltration is of any major significance to ground water recharge in the area since the model only covers the top 5 m and the infiltration rates are minor. These results consist with the findings of Gonzales Amaya et al. (2018). The model is yet useful in its contribution to an eventual water balance model of the Chocaya basin and show that more surveys are needed to understand where the replenishment of the underlying alluvial aquifers originates.

Based on the formation process of alluvium it is assumed that the constructed models in Hydrus-ID are representative of the whole plain. Alluvium is distributed by water as lake or river sediments and as the water flow rate is variable over periods of time, alluvial soils are often made up of several distinct layers as seen in the riverbed running through the alluvial plain in Chocaya basin. The constructed models only take the top part of the unsaturated zone in account thus implying that the alluvial deposit is rather homogenous over the plain.

6. Conclusions

Infiltration rate estimation methods are important in the development and management of sustainable groundwater resources. Field investigations have been performed in order to determine the water infiltration rate and the hydraulic conductivity in the unsaturated zone of Chocaya basin. The double ring infiltrometer tests and resulting hydraulic conductivity (K_s) using Philip's equation all showed a good fit and reasonable results within a relatively small range. In the Chocaya basin top 1m layer, infiltration rate and K_s ranges between 1.8×10^{-6} – 1.4×10^{-5} m/s and 2.6×10^{-6} – 2.1×10^{-5} m/s respectively. When using the soil parameters obtained from lab analysis K_s ranged between 3.9×10^{-6} – 2.1×10^{-5} m/s. The results from Beyer and Hazen equations are not considered since they provided unreasonable values. This is believed to be caused by less accurate soil analysis.

The particle size distribution and electrical resistivity tomography (ERT) contained several contradictions at different locations. Some locations with a higher electrical resistivity have a larger fraction of finer sediments and some present the opposite. This indicates that ERT measurements are site specific and it is difficult to find correlations that can be used further in other projects. ERT is, however, a useful tool to observe local soil stratification. It was further recognized that the Rosetta module offers a simple and relatively quick way of predicting soil hydraulic properties.

The resulting bottom flux from the Hydrus-1D models are largely dependent on initial soil water content (θ_i). It is therefore important to properly acquire this parameter prior to creating a model. The constructed model was seen representative of the area due to that the formation process of alluvium have created distinct homogenous layers in the field and that the model only takes the top part of the unsaturated zone in account. It can however be concluded that the percolated water volume at 5 m is of minor importance for groundwater recharge in Chocaya basin.

7. Recommendations

This study discussed the rainwater infiltration in Chocaya basin alluvial plain. To increase the knowledge of the infiltration process and to improve the accuracy of the model more surveys are needed in the area. Here follow recommendations for further investigations;

-   It would be suggested to conduct ERT tests to a depth of 50 m in order to capture the soil stratigraphy deeper in the alluvial plain in order to have the ability to distinguish possibly occurring semi-impermeable layers.

-   More ERT and DRI tests and collected soil samples at each of the locations are recommended. These could improve the data reliability for the soil parameter input values.

-   Because of the large amounts of coarse-grained material in the field, it would be necessary to collect larger soil samples to be analysed so it can be conceivable to assume that they represent the alluvial plain.

-   It would have been advantageous to install soil moisture sensors in the alluvial plain as an evaluation of the accuracy of the simulation model. However, this would imply contracting an excavator machinery as the soil was difficult to dig due to its dryness and high content of gravel and stones.

8. References

Alley, W. M. (2009). Ground Water. In G. E. Likens (Ed.), *Encyclopedia of Inland Waters* (pp. 684-690). Oxford: Academic Press.

Aning, A., Tucholka, P., & Danuor, S. (2013). 2D Electrical Resistivity Tomography (ERT) Survey using the Multi-Electrode Gradient Array at the Bosumtwi Impact Crater, Ghana.

AQUASTAT, F. a. A. O. (2020). Renewable internal freshwater resources per capita (cubic meters). Retrieved from https://databank.worldbank.org/source/world-development-indicators

ASTM D422-63. (2007). *Standard Test Method for Particle-Size Analysis of Soils*. Retrieved from West Conshohocken, PA: http://www.astm.org/cgi-bin/resolver.cgi?D422-63(2007)e2

Bing, Z. (2019). Electrical Resistivity Tomography: A Subsurface-Imaging Technique. doi:10.5772/intechopen.81511

Campbell Scientific, I. (2020). CR300 - Measurement and Control Datalogger. Retrieved from https://www.campbellsci.com/cr300

Cossio, V., Bustamante, R., & Skielboe, T. (2010). *Conflict and cooperation in local water governance – inventory of local water-related events in Tiraque District, Bolivia*. Retrieved from www.jstor.org/stable/resrep13323

Dahlin, T. (2001). The development of DC resistivity imaging techniques. *Computers & Geosciences, 27*(9), 1019-1029. doi:https://doi.org/10.1016/S0098-3004(00)00160-6

Dirección de Planificación y Gestión Integral del Agua (DGIA). (2014). *Agenda del Agua Cochabamba (2015-2025)*. Retrieved from

Droogers, P., & Allen, R. G. (2002). Estimating Reference Evapotranspiration Under Inaccurate Data Conditions. *Irrigation and Drainage Systems, 16*(1), 33-45. doi:10.1023/A:1015508322413

Fatehnia, M., Tawfiq, K., & Ye, M. (2016). Estimation of saturated hydraulic conductivity from double-ring infiltrometer measurements. *European Journal of Soil Science, 67*(2), 135-147. doi:10.1111/ejss.12322

Feki, M., Ravazzani, G., Ceppi, A., Milleo, G., & Mancini, M. (2018). Impact of Infiltration Process Modeling on Soil Water Content Simulations for Irrigation Management. *Water, 10*(7), 850. Retrieved from https://www.mdpi.com/2073-4441/10/7/850

Fodor, N., Sandor, R., Orfanus, T., Lichner, L., & Rajkai, K. (2011). Evaluation method dependency of measured saturated hydraulic conductivity. *Geoderma, 165*(1), 60-68. doi:10.1016/j.geoderma.2011.07.004

Genuchten van, M. (1980). A Closed-form Equation for Predicting the Hydraulic Conductivity of Unsaturated Soils1. *Soil Science Society of America Journal, 44*. doi:10.2136/sssaj1980.03615995004400050002x

Gómez, E., Broman, V., Dahlin, T., Barmen, G., & Rosberg, J.-E. (2019). Quantitative estimations of aquifer properties from resistivity in the Bolivian highlands. *H2Open Journal, 2*(1), 113-124. doi:10.2166/h2oj.2019.007

Gonzales Amaya, A. (2019). Characterisation of Aquifers in Bolivia. Retrieved from https://bolivia.blogg.lu.se/projects/chocaya/introduction/

Gonzales Amaya, A., Barmen, G., & Muñoz, G. (2018). A Multidisciplinary Approach for Clarifying the Recharge Processes and Origin of Saline Water in the Semi-Arid Punata Alluvial fan in Bolivia. *Water, 10*(7), 946. Retrieved from https://www.mdpi.com/2073-4441/10/7/946

Gonzales Amaya, A., Villazon, M. F., & Willems, P. (2018). Assessment of rainfall variability and its relationship to ENSO in a sub-Andean watershed in central Bolivia. *Water (Switzerland), 10*(6). doi:10.3390/w10060701

Guidline Geo. (2007). Erigraph 2.2. Retrieved from https://www.guidelinegeo.com/wp-content/uploads/2016/03/Erigraph_user_guide.pdf

Guidline Geo. (2009). EriViz. Retrieved from https://www.guidelinegeo.com/wp-content/uploads/2016/07/User-guide-to-EriViz.pdf

Hargreaves, G. H. (1994). Defining and Using Reference Evapotranspiration. *Journal of Irrigation and Drainage Engineering, 120*(6), 1132-1139. doi:doi:10.1061/(ASCE)0733-9437(1994)120:6(1132)

Heinz, J., Kleineidam, S., Teutsch, G., & Aigner, T. (2003). Heterogeneity patterns of Quaternary glaciofluvial gravel bodies (SW-Germany): application to hydrogeology. *Sedimentary Geology, 158*(1), 1-23. doi:https://doi.org/10.1016/S0037-0738(02)00239-7

Houston, J. (2002). Groundwater recharge through an alluvial fan in the Atacama Desert, northern Chile: mechanisms, magnitudes and causes. *Hydrological Processes, 16*, 3019-3035. Retrieved from https://ui.adsabs.harvard.edu/abs/2002HyPr...16.3019H

Hung, Y.-C., Lin, C.-P., Lee, C.-T., & Weng, K.-W. (2019). 3D and Boundary Effects on 2D Electrical Resistivity Tomography. *Applied Sciences, 9*, 2963. doi:10.3390/app9152963

INE, I. N. d. E. (2016). *Población de Cochabamba llega a 1.916.000 habitantes al 2016*. La Paz, Bolivia Retrieved from https://www.ine.gob.bo/index.php/component/k2/item/416-poblacion-de-cochabamba-llega-a-1-916-000-habitantes-al-2016?highlight=WyJjb2NoYWJhbWJhIl0=

Kirsch, R., & Yaramanci, U. (2009). Geophysical characterisation of aquifers. In R. Kirsch (Ed.), *Groundwater Geophysics: A Tool for Hydrogeology* (pp. 491-509). Berlin, Heidelberg: Springer Berlin Heidelberg.

Ministerio de Medio Ambiente y Agua (MMAyA). (2014). *Plan maestro metropolitano de agua y saneamiento de Cochabamba, Bolivia* (Vol. Informe Final).

Mollerup, M. (2007). Philip's infiltration equation for variable-head ponded infiltration. *Journal of Hydrology, 347*(1-2), 173-176. doi:10.1016/j.jhydrol.2007.09.015

Mualem, Y. (1976). A new model for predicting the hydraulic conductivity of unsaturated porous media. *Water Resources Research, 12*(3), 513-522. doi:10.1029/WR012i003p00513

Ohlsson, L. (2000). *Livelihood conflicts : linking poverty and environment as causes of conflict*: Sida, Department for Natural Resources and the Environment.

Onset, C. C. (2020a). EC5 Soil Moisture Smart Sensor. Retrieved from https://www.onsetcomp.com/products/sensors/s-smc-m005

Onset, C. C. (2020b). HOBO Rain Gauge (Metric) Data Logger Part RG3-M. Retrieved from https://www.onsetcomp.com/products/data-loggers/rg3-m

Radcliffe, D. E., & Simunek, J. (2010). *Soil Physics with HYDRUS Modeling and Applications* (1st Edition ed.). Boca Raton: FL: CRC Press/Taylor & Francis.

Reichling, K., Raupach, M., & Klitzsch, N. (2015). Determination of the distribution of electrical resistivity in reinforced concrete structures using electrical resistivity tomography. *Materials and Corrosion, 66*(8), 763-771. doi:DOI: 10.1002/maco.201407763.

Renner, S., & Velasco, C. (2000). Geology and Hydrogeology of the Central Valley of Cochabamba. German Bolivian Agreement on Groundwater (CABAS). *Boletin del Servicio National de Geologia y Mineria, 35*.

Ritter, A., Hupet, F., Muñoz-Carpena, R., Lambot, S., & Vanclooster, M. (2003). Using inverse methods for estimating soil hydraulic properties from field data as an alternative to direct methods. *Agricultural Water Management, 59*, 77-96. doi:10.1016/S0378-3774(02)00160-9

Sakata, Y., & Ikeda, R. (2013). Depth dependence and exponential models of permeability in alluvial-fan gravel deposits. *Hydrogeology Journal, 21*(4), 773-786. doi:10.1007/s10040-013-0961-8

Scanlon, B. R., Healy, R. W., & Cook, P. G. (2002). Choosing appropriate techniques for quantifying groundwater recharge. *Hydrogeology Journal, 10*(1), 18-39. doi:10.1007/s10040-001-0176-2

Şen, Z. (2015). Chapter Six - Climate Change, Droughts, and Water Resources. In Z. Şen (Ed.), *Applied Drought Modeling, Prediction, and Mitigation* (pp. 321-391). Boston: Elsevier.

Shiraki, S., Thu, A. K., Matsuno, Y., & Shinogi, Y. (2019). Evaluation of infiltration models and field-saturated hydraulic conductivity in situ infiltration tests during the dry season. *Paddy and Water Environment, 17*(4), 619-632. doi:10.1007/s10333-018-00688-w

Šimůnek, J., Šejna, M., Saito, H., Sakai, M., & Genuchten, M. T. v. (2013). *The HYDRUS-1D Software Package for Simulating the One-Dimensional Movement of Water, Heat, and Multiple Solutes*

in Variably-Saturated Media. Retrieved from Riverside, California: https://www.pc-progress.com/Downloads/Pgm_hydrus1D/HYDRUS1D-4.17.pdf

Soilmoisture Equipment Corp. (2009). *2830K1 Double Ring Infiltrometer Kit, Operating Instructions*. Retrieved from Santa Barbara, CA: https://www.soilmoisture.com/pdfs/Resource_Instructions_0898-2830_2830K1%20Double%20Ring%20Infiltrometer.pdf

Solinst Canada Ltd. (2019). 1.1.2 Barologger Edge. Retrieved from https://www.solinst.com/products/dataloggers-and-telemetry/3001-levelogger-series/operating-instructions/user-guide/1-introduction/1-1-2-barologger-edge.php

Standardiseringskommissionen i Sverige (SIS). (1992). Geotekniska provningsmetoder - Kornfördelning - Siktning. In.

Stephens, D., Hsu, K.-C., Prieksat, M., Ankeny, M., Blandford, N., Roth, T., . . . Whitworth, J. (1998). A comparison of estimated and calculated effective porosity. *Hydrogeology Journal, 6*, 156-165. doi:10.1007/s100400050141

Turesson, A. (2006). Water content and porosity estimated from ground-penetrating radar and resistivity. *Journal of Applied Geophysics, 58*(2), 99-111. doi:https://doi.org/10.1016/j.jappgeo.2005.04.004

UI, U. I. (2019). Sociala förhållanden. Retrieved from https://www.ui.se/landguiden/lander-och-omraden/sydamerika/bolivia/sociala-forhallanden/

UN. Secretary-General. (2018). *Progress towards the Sustainable Development Goals : report of the Secretary-General*. Retrieved from New York: http://digitallibrary.un.org/record/1627573/files/E_2018_64-EN.pdf

Wang, J.-P., François, B., & Lambert, P. (2017). Equations for hydraulic conductivity estimation from particle size distribution: A dimensional analysis. *Water Resources Research, 53*(9), 8127-8134. doi:10.1002/2017wr020888

World Weather Online. (2019). Cochabamba Monthly Climate Averages. Retrieved from https://www.worldweatheronline.com/cochabamba-weather-averages/cochabamba/bo.aspx

Zhu, L., Gong, H., Dai, Z., Guo, G., & Teatini, P. (2017). Modeling 3-D permeability distribution in alluvial fans using facies architecture and geophysical acquisitions. *Hydrol. Earth Syst. Sci., 21*(2), 721-733. doi:10.5194/hess-21-721-2017

9. Appendices

Appendix A – Soil Sample Data

Appendix A includes data from soil samples, an example of calculated particle size distribution and the obtained parameters from the Rosetta module.

Location Information
Location depth (m), field names and Location coordinates (WGS 84 Web Mercator) are seen in Table A 1.

Table A 1: Locations coordinates and depth (m) of soil samples.

Location	Depth [m]	Location in field [Name]	Coordinates [WGS 84 Web Mercator]
1	0	Potreros	-17.320169, -66.308237
1	0.6	Potreros	-17.320169, -66.308237
1	1.05	Potreros	-17.320169, -66.308237
2	0	Potreros	-17.320546, -66.308123
2	0.6	Potreros	-17.320546, -66.308123
3	0	Marquina (alluvial plain)	-17.337064, -66.278688
4	0	Marquina (alluvial plain)	-17.344816, -66.279911
5	0.05	Marquina (riverbed)	-17.347033, -66.275659
5	2.6	Marquina (riverbed)	-17.347033, -66.275659
5	3.3	Marquina (riverbed)	-17.347033, -66.275659
6	0	Marquina (alluvial plain)	-17.350705, -66.280372

Example of Particle Size Distribution Calculation
Parameters for the fabricated particle size distribution (PSD) curve (for Location 1, *0 m*) with sieve size, measured weight and calculated accumulated weight are displayed in Table A 2.

Table A 2: Sieve size and calculated particle size distributions for Location 1 (0.0, 0.6, 1.05 m), 2 (0.0, 0.6 m) and 5 (0.05, 2.6, 3.3 m).

Sieve size [mm]	Location 1 *(0m)*	Weight [%]	Accumulated Weight	Accumulated % Passing
75	0.0	0.0	0.0	100.0
50	0.0	0.0	0.0	100.0
37.5	358.5	15.2	358.5	84.8
25	203.4	8.6	561.9	76.1
19	145.9	6.2	707.8	69.9
12.5	154.4	6.6	862.2	63.3
9.5	59.0	2.5	921.2	60.8
4.75	144.3	6.1	1065.5	54.7
2.36	114.1	4.9	1179.6	49.8
0.063	527.4	22.4	1707.0	27.4
0.004	421.9	17.9	2128.9	9.5
PAN	222.7	9.5	2351.6	0.0

Soil Analysis

The physical soil analysis from Laboratorio de Suelos y Aguas with the used parameters %(sand, silt and clay), bulk density (ρ_b), wilting point (Θ_{wp}) and porosity (ϕ) are displayed in Table A 3.

Table A 3: Physical analysis of soil samples obtained from Laboratorio de Suelos y Agua, UMSS

UNIVERSIDAD MAYOR DE SAN SIMON
FAC. de CS. AGRICOLAS, PECUARIAS y FORESTALE
   "Martín Cárdenas"
Dpto. de Ingeniería Agrícola

LABORATORIO DE SUELOS Y AGUAS

ANALISIS FISICO DE SUELOS

Interesado: LABORATORIO DE HIDRAULICA - UMSS
Proyecto: CARACTERIZACION CUENCA CHOCAYA
Responsable: Ing. Andrès Gonzales
Procedencia: Cuenca Choacaya, Cochabamba.

Nº Lab.	Identific. Perfil No.	DEPTH m	Y %	L %	A %	TEXTURE	BULK DENSITY g/cm3	REAL DENSITY g/cm3	C.H. cm/h	FIELD CAPACITY %	WILTING POINT %	POROSITY %	AVAILABLE WATER %
1026	Location 1	0,05	19	36	45	F	1,18	2,45		18,24	9,60	51,85	8,63
1027	Location 1	0,5	13	31	56	FA	1,63	2,65		14,66	7,36	38,51	7,31
1028	Location 1	1,05	11	28	61	FA	1,26	2,70		13,39	6,56	53,19	6,83
1029	Location 2	0,05	11	28	61	FA	1,09	2,70		13,41	6,57	59,47	6,84
1030	Location 2	0,5	21	36	43	F	1,34	2,52		19,08	10,13	46,69	8,95
1031	River Bottom		18	29	53	FA	1,62	2,71		16,50	8,51	40,15	7,99
1032	River Midal		11	29	60	FA	1,61	2,75		13,63	6,71	41,49	6,92
1033	River Upper		11	19	69	FA	1,80	2,72		12,31	5,88	33,67	6,43

Y= day   C.H.= hydraulic conductivity (permeability)
L = silt
A = sand

Fecha: Cbba., 16 Diciembre de 2019

Dirección: Av. Petrolera Km 5, Tel. 4237506-Fax: 4762385; Email: lab.suelos@agr.umss.edu.bo.

Rosetta Module

The parameters (Θ_r and Θ_s, *alpha*, *n* and K_s) predicted from the PSDs by the Rosetta module in Hydrus-1D are displayed in Table A 4. Location 2 (0 m) obtained the highest K_s and Location 5 (3.3 m) the lowest. The input parameters (porosity (ϕ), field capacity (Θ_{fc}), %(sand, silt and clay) and bulk density (ρ_b)) for the different locations are seen in Appendix A, Table A 3.

Table A 4. The predicted parameters for Location 1, 2 and 5 from the Rosetta module.

Location	Θ_r [-]	Θ_s [-]	*alpha* [1/cm]	*n* [-]	K_s [m/s]
Loc 1 *(0 m)*	0.04	0.46	0.05	1.40	6.64×10^{-6}
Loc 1 *(0.6 m)*	0.03	0.33	0.04	1.40	4.22×10^{-6}
Loc 1 *(1.05 m)*	0.03	0.43	0.06	1.48	1.52×10^{-5}
Loc 2 *(0 m)*	0.03	0.48	0.07	1.48	2.08×10^{-5}
Loc 2 *(0.6 m)*	0.05	0.41	0.04	1.38	4.28×10^{-6}
Loc 5 *(0.05 m)*	0.03	0.30	0.05	1.38	4.85×10^{-6}
Loc 5 *(2.6 m)*	0.03	0.34	0.05	1.42	5.36×10^{-6}
Loc 5 *(3.3 m)*	0.04	0.34	0.04	1.37	3.91×10^{-6}

Appendix B – Soil Water Content (θ)

Precipitation and Soil Water Content

Precipitation and soil water content (θ) obtained from soil moisture sensors at (0.1, 0.45, 0.8 and 1.05 m depths) over time (2019-10-20 – 2020-01-17) at Location 1 are seen in Figure B 1. The peaks in θ follows the precipitation events with some delay. Hence it was credible to presume that the equipment worked properly. The peak is most abundant at depth 0.1 m and decreasing with depth.
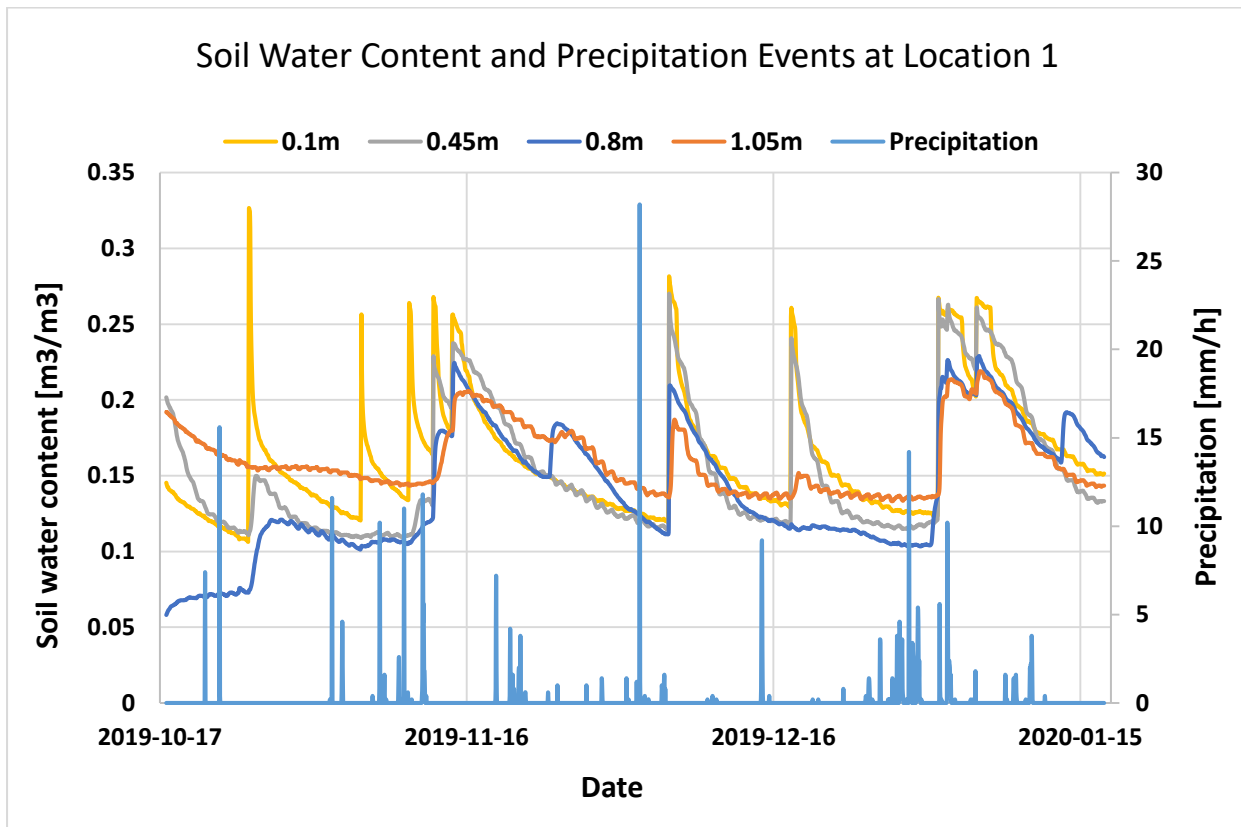

Figure B 1. Precipitation and soil water content (0.1, 0.45, 0.8 and 1.0 m depth) at Location 1 between the dates 2019-10-20 – 2020-01-17.

Simulated Soil Water Content

The θ result for the two Hargreaves models for Location 1 (depths 0.45 and 0.8 m) are seen in Figure B 2. The inverse optimization model succeeded to capture the increase/decrease in θ between rain events better for depth 0.8 m. At 0.45 m the two models displayed equal performance. However, the peaks in θ due to large precipitation events are still not captured to a greater extent at 0.45 m.
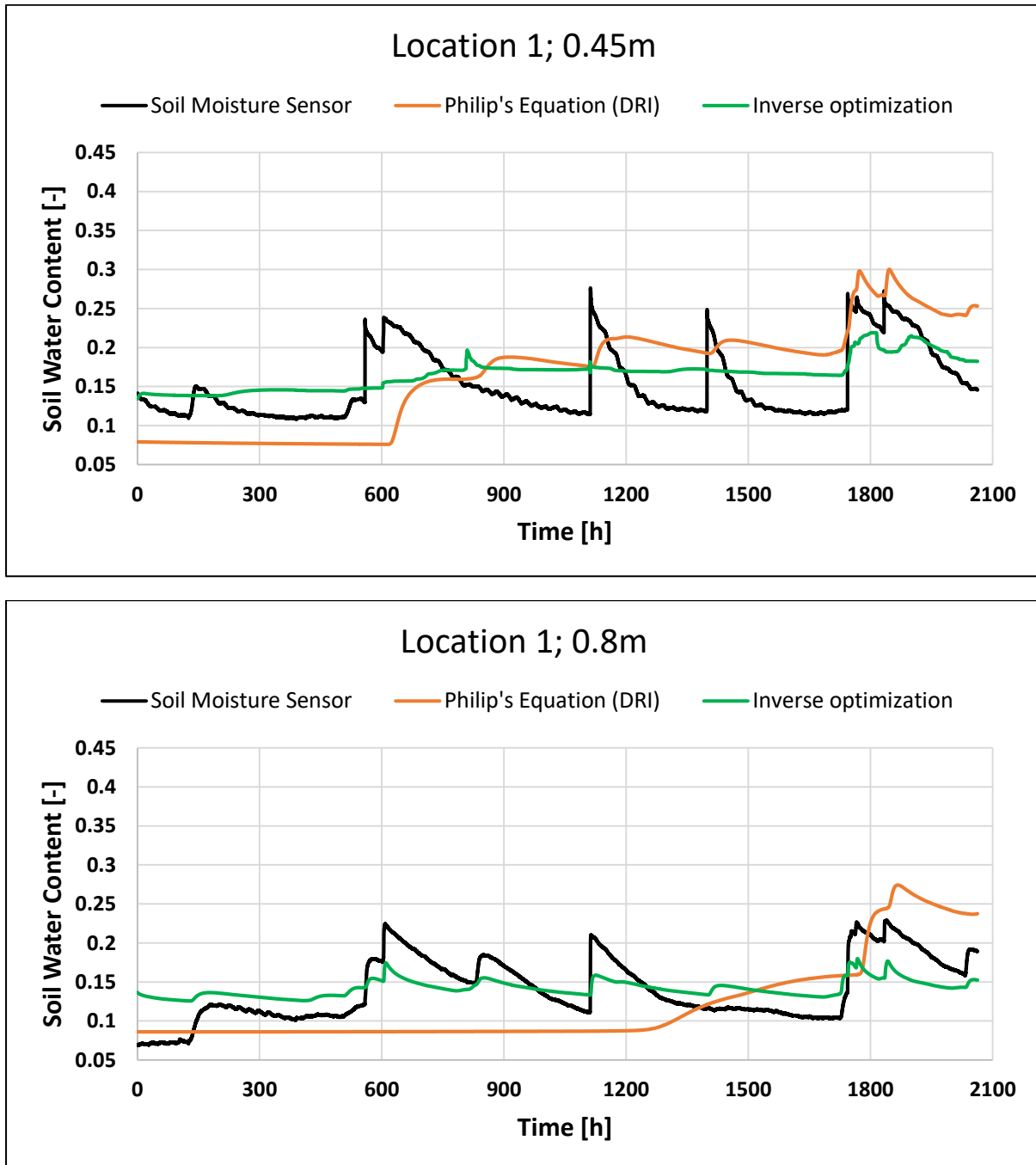

Figure B 2. Measured soil water content (θ) (black) and simulated θ with the two Hargreaves models with the parameter; DRI (orange) and Inverse optimization (green) for depths 0.45 m (top) and 0.8 m (bottom).

Appendix C – Hydrus-1D Model Setup

The constructed model for Location 1 with the three materials are seen in (Figure C 1, left). A total of 4 nodes were introduced in the model at the same depth as the installed soil moisture sensors (0.1, 0.45, 0.8 and 1.05 m depths) facilitating the comparison between the measured and simulated soil water content (θ). The constructed model for the alluvial plain with the same material distribution as Location 1 but with an additional material layer between 4-5 m are seen in Figure C 1 (right). A total of 5 nodes were introduced in the model at (0.05, 0.5, 1.0, 2.0 and 4.0 m depths).
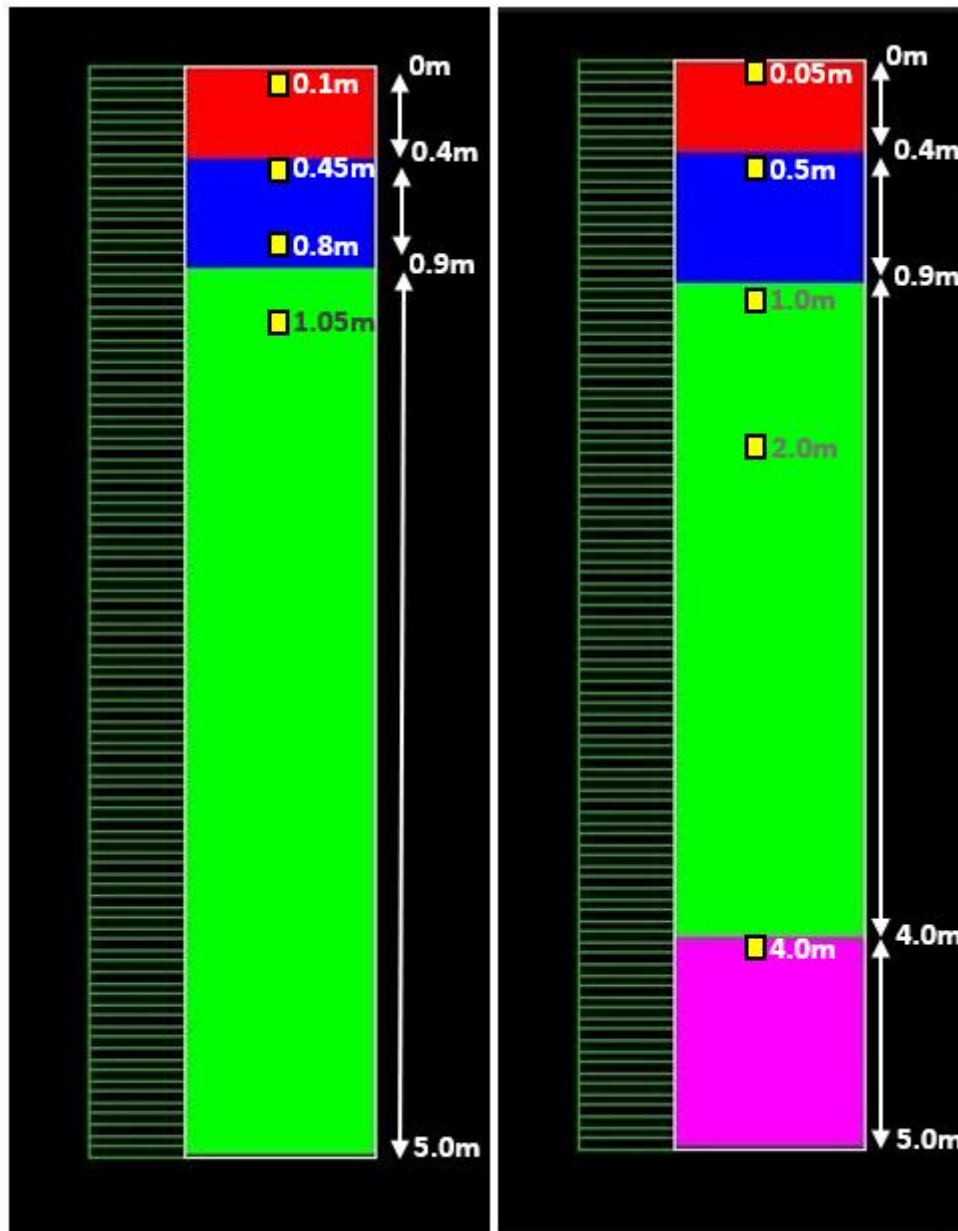

Figure C 1. Schematic figure over the distribution of the three materials for Location 1 (left) and the distribution of the four materials for the alluvial plain (right).

Input Parameters

Table C 1 and Table C 2 shows the input parameters (Θ_r, Θ_s, *alpha, n*, K_s and *I*) for Material 1, 2 and 3 at Location 1. The parameters were obtained from Philip's equation (DRI) and Rosetta module (Table C 1) and from the inverse optimization model (Table C 2). The yellow row shows the specific input parameters for Material 4 used in the simulation over the alluvial plain with parameters obtained from the Rosetta module (Location 5, 3.3 m, (Table A 4)).

Table C 1. Parameters obtained from Philip's equation (DRI) and Rosetta module used in the Hargreaves equation for Location 1 and the alluvial plain.

Material	Θ_r [-]	Θ_s [-]	*alpha* [1/cm]	*n* [-]	K_s [m/s]	*I* [-]
1	0.04	0.5	0.05	1.40	2.1×10^{-5}	0.5
2	0.03	0.3	0.04	1.40	3.9×10^{-6}	0.5
3	0.03	0.4	0.06	1.48	1.5×10^{-5}	0.5
4	0.04	0.3	0.04	1.37	3.8×10^{-6}	0.5

Table C 2. Parameters obtained from the inverse optimization method used in the Hargreaves equation for Location 1 and the alluvial plain.

Material	Θ_r [-]	Θ_s [-]	*alpha* [1/cm]	*n* [-]	K_s [m/s]	*I* [-]
1	0.07	0.2	0.07	1.31	8.5×10^{-6}	0.5
2	0.04	0.2	0.07	1.3	5.6×10^{-5}	0.5
3	0.07	0.2	0.07	1.3	2.2×10^{-6}	0.5
4	0.04	0.3	0.04	1.37	3.8×10^{-6}	0.5

Appendix D - General Input Parameters for Hydrus-1D

Main Processes
Simulate: Water flow

Geometry Information
Length units: cm
Number of soil materials: 3 *(Location 1)* / 4 *(the alluvial plain)*
Number of layers for mass balances: 1
Decline from vertical axes: 1
Depth of the soil profile: 500

Time Information
Time units: hours
Initial time: 0
Final time: 10000
Initial time step: 0.024
Minimum time step: 0.00024
Maximum time step: 120
Number of time-variable boundary conditions: 10000
Number of meteorological records: 10000
Hargreaves Formula

Iteration Criteria
Maximum number of iterations: 10
Water content tolerance: 0.001
Pressure Head Tolerance: 1
Lower optimal iteration range: 7
Lower time step multiplication factor: 1.3
Upper time step multiplication factor: 0.7
Lower limit of the tension interval: 1e-006
Upper limit of the tension interval: 10000

Soil Hydraulic Model
Single porosity models: van Genuchten-Maulem
Hysteresis: No hysteresis

Water Flow Boundary Conditions
Upper boundary condition: Atmospheric BC with surface layer
Lower boundary condition: Free drainage
Initial condition: In water contents
Max h at soil surface: 0

Time Variable Boundary Conditions
Precipitaion: Meteorological data from Chaupisuyo
HCritA [cm]: -50000

Meteorological Parameters
Radiation: Potential radiation
Latitude: -17.4223

Meteorological Conditions
T_max and T_min: Temperature data from Chaupisuyo

Appendix E – Simulated Results over the Alluvial Plain

Initial Soil Water Content: (0.1)

The simulated θ for 5 observation nodes in the model (FM1) where θ_i had been set to 0.1 throughout the profile are seen in (Figure E 1). The observation nodes are at depths; N1= 0.05m.b.s, N2=0.5 m.b.s, N3=1.0 m.b.s, N4=2.0 m.b.s and N5=4.0 m.b.s. The node at 4 m does not see any changes in θ during the simulated period (Nov, 2018 – Jan, 2020).
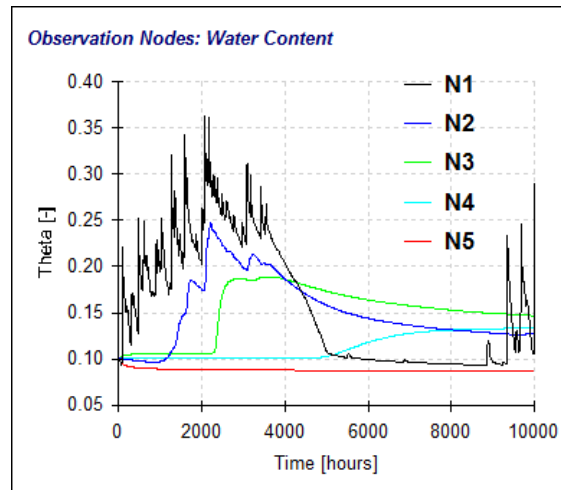

Figure E 1. Water contents (θ) from DRI/Rosetta model in the simulated soil profile for the period (Nov, 2018 – Jan, 2020) at observation nodes at four different depths: N1= 0.05 m.b.s, N2=0.5 m.b.s, N3=1.0 m.b.s, N4=2.0 m.b.s and N5=4.0 m.b.s.

Initial Soil Water Content: gradual (0.1-0.2)

The simulated θ for 5 observation nodes for the two models, (FM2 (left) and IM2 (right)) where θ_i had been set to gradual (0.1-0.2) throughout the profile are seen in (Figure E 2). The observation nodes are at depths; N1= 0.05 m, N2=0.5 m, N3=1.0 m, N4=2.0 m and N5=4.0 m. All nodes experience fluctuations in soil water content during the simulated period (Nov, 2018 – Jan, 2020).
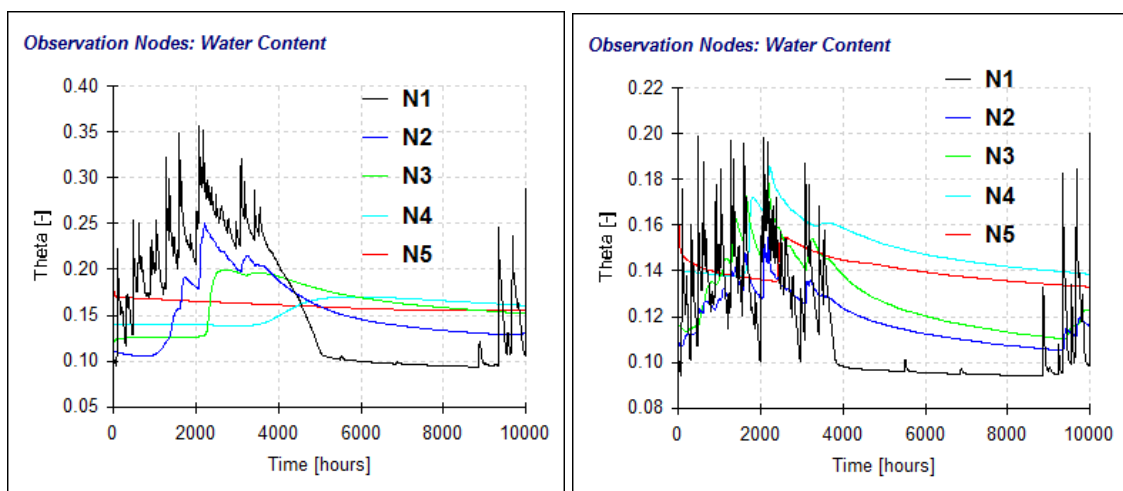

Figure E 2. Water contents (θ) from FM2 (left) and IM2 (right) in the simulated soil profile for the period (Nov, 2018 – Jan, 2020) at observation nodes at four different depths: N1= 0.05 m.b.s, N2=0.5 m.b.s, N3=1.0 m.b.s, N4=2.0 m.b.s and N5=4.0 m.b.s.